Bud23 promotes the progression of the Small Subunit Processome to the pre-40S ribosome in *Saccharomyces cerevisiae*

Joshua J. Black[1], Richa Sardana[1, †], Ezzeddine W. Elmir[1], Arlen W. Johnson[1, *]

[1] Department of Molecular Biosciences, The University of Texas at Austin, Austin, Texas, United States of America

[†] Current Address: Department of Molecular Biology and Genetics, Weill Institute for Cell and Molecular Biology, Cornell University, Ithaca, NY

Running tittle: The role of Bud23 in 40S maturation.

*Corresponding author

Email: arlen@austin.utexas.edu (AWJ)

Abstract

The first metastable assembly intermediate of the eukaryotic ribosomal small subunit (SSU) is the SSU Processome, a large complex of RNA and protein factors that is thought to represent an early checkpoint in the assembly pathway. Transition of the SSU Processome towards continued maturation requires the removal of the U3 snoRNA and biogenesis factors as well as ribosomal RNA processing. While the factors that drive these events are largely known, how they do so is not well understood. The methyltransferase Bud23 has a role during this transition, but its function, beyond the nonessential methylation of 18S rRNA, is not characterized. Here, we have carried out a comprehensive genetic screen to understand Bud23 function. We identified 67 unique extragenic *bud23*Δ-suppressing mutations that mapped to genes encoding the SSU Processome factors *DHR1*, *IMP4*, *UTP2* (*NOP14*), *BMS1* and the SSU protein *RPS28A*. These factors form a physical interaction network that links the binding site of Bud23 to the U3 snoRNA and many of the suppressing mutations weaken protein-protein and protein-RNA interactions. Importantly, this network links Bud23 to the GTPase Bms1 and the RNA helicase Dhr1. Bms1 is thought to drive conformational changes to promote rRNA cleavage, and we previously showed that Dhr1 is required for unwinding the U3 snoRNA. Moreover, particles isolated from cells lacking Bud23 accumulated late SSU Processome factors and pre-rRNAs not cleaved at sites A1 and A2. We propose a model in which Bud23 dissociates factors surrounding its binding site to promote SSU Processome progression.

Author summary

Ribosomes are the molecular machines that synthesize proteins and are composed of a large and a small subunit which carry out the essential functions of polypeptide synthesis and mRNA decoding, respectively. Ribosome production is tightly linked to cellular growth as cells must produce enough ribosomes to meet their protein needs. However, ribosome assembly is a metabolically expensive pathway that must be balanced with other cellular energy needs and regulated accordingly. In eukaryotes, the small subunit (SSU) Processome is a metastable intermediate that ultimately progresses towards a mature SSU through the release of biogenesis factors. The decision to progress the SSU Processome is thought to be an early checkpoint in the SSU assembly pathway, but what drives this checkpoint is unknown. Previous studies suggest that Bud23 plays an uncharacterized role during SSU Processome progression. Here, we used a genetic approach to understand its function and found that Bud23 is connected to a network of factors that stabilize the particle. Interestingly, two of these factors are enzymes that facilitate structural rearrangements needed for progression. We conclude that Bud23 promotes the release of factors surrounding its binding site to drive rearrangements during the progression of the SSU Processome.

Introduction

Ribosomes are the molecular machines that translate the genetic code. Each ribosome is composed of a small subunit (SSU) that coordinates mRNAs and tRNAs for decoding and a large subunit (LSU) that catalyzes peptide bond formation. In the eukaryotic model organism *Saccharomyces cerevisiae*, the LSU, or 60S, contains three rRNAs (25S, 5.8S and 5S) and 46 ribosomal proteins (r-proteins), whereas the SSU, or 40S, has the 18S rRNA and 33 r-proteins [1].

65 The subunits are produced by an energetically expensive and dynamic assembly pathway
66 requiring more than 200 *trans*-acting biogenesis factors (reviewed in [2–5]). Ribosome assembly
67 begins in the nucleolus with the synthesis of the primary 35S rRNA transcript and the 5S rRNA.
68 The primary transcript contains the 18S, 5.8S, and 25S rRNAs and four spacer regions that are
69 removed during ribosome assembly: two external transcribed spacers (ETS) and two internal
70 transcribed spacers (ITS) (Fig. S1). The r-proteins and the biogenesis factors assemble on the rRNA
71 in a hierarchical order [6–10], most of which promote the correct architecture of the subunits by
72 chaperoning and modifying the rRNA while others drive structural rearrangements and the
73 removal of the spacer regions.

74 Because the pre-18S rRNA is encoded in the 5'-portion of the primary transcript the initial
75 folding of the pre-rRNA is dedicated to SSU assembly. These co-transcriptional nucleolar events
76 lead to assembly of the SSU Processome (sometimes referred to as a 90S pre-ribosome) [8,11,12].
77 The SSU Processome serves two primary roles: 1) promote the formation of the SSU architecture
78 and 2) process the pre-rRNA at sites A0 and A1, to remove the 5' ETS, and at site A2, to separate
79 the SSU and LSU precursors (reviewed in [13,14]). Recent high-resolution structures of the
80 complete SSU Processome revealed a large metastable assemblage of 15 r-proteins and about 50
81 biogenesis factors on the 5' ETS and pre-18S rRNAs [15–17]. The 18S rRNA is divided into the 5',
82 central, 3' major, and 3' minor domains (Fig. S2) that fold independently as the SSU Processome
83 assembles [15–19]. In the SSU Processome, these RNA domains are scaffolded by a multitude of
84 biogenesis factors, the 5' ETS ribonucleoprotein complex (RNP), and U3 snoRNA that prevent
85 their collapse into the densely packed structure of the subsequent pre-40S and mature 40S
86 particles. A correctly assembled SSU Processome ultimately transitions to the pre-40S [20] which

87 requires the release of most of these biogenesis factors, including U3 and 5' ETS RNP, as well as
88 the aforementioned endonucleolytic cleavages of the pre-rRNA. This transition and the
89 coordinated disassembly of the SSU Processome allows large architectural rearrangements to
90 occur that yield the pre-40S and likely release it into the nucleoplasm for continued maturation.
91 While recent structural and molecular analysis of the SSU Processome have brought its assembly
92 into focus, there remains a dearth of understanding about the events and mechanisms driving its
93 transition into the pre-40S.

94 Early recruitment of the U3 snoRNA is crucial for the formation and function of the SSU
95 Processome [7,11,21–26]. Structural analyses of the SSU Processome show that the box C/D U3
96 snoRNA threads into the core of the complex where it spatially separates the rRNA domains and
97 scaffolds biogenesis factors [15,16]. Two regions of U3, referred to as the 5' and 3' hinges,
98 hybridize to the 5' ETS RNA while its Box A' and Box A regions hybridize to the pre-18S rRNA,
99 henceforth U3-18S heteroduplexes. Notably, Box A hybridizes with helix 1 of 18S, precluding the
100 formation of the Central Pseudoknot (CPK) of the SSU [15,17]. The CPK is a universally conserved
101 feature of the SSU formed by long-range, non-canonical base-pairing between helices 1 and 2
102 that allows the four rRNA domains to compact onto one another (Fig. S2), and generates the
103 environment necessary to establish the decoding center [1,27]. Because U3 blocks CPK
104 formation, the release of U3 is a critical, irreversible step in the maturation of the SSU [14,28].
105 The unwinding of U3 is catalyzed by the DEAH/RHA helicase Dhr1 [29] which is activated by the
106 SSU Processome factor Utp14 [30–32]. Mutational analysis identified a short loop of Utp14 that
107 is necessary and sufficient for the activation of Dhr1 *in vitro* [30,32], and deletion or significant
108 mutation of this loop phenocopies a catalytic *dhr1* mutant *in vivo* [30]. How Utp14 times the

109 activation of Dhr1 remains unknown, and neither Dhr1 nor the activation loop of Utp14 have
110 been resolved in SSU Processome structures [15,16]. RNA crosslinking and structural analysis
111 indicate that Utp14 binds simultaneously to the U3 and 5' ETS RNAs, as well as the central domain
112 and 5'- and 3'-ends of the pre-18S rRNA, suggesting that Utp14 is uniquely positioned to time
113 Dhr1 activation by monitoring completion of transcription of the pre-18S rRNA [15,16,33].

114 The endonucleolytic cleavages within the rRNA at sites A1 and A2 are also irreversible
115 steps that occur around the time of the transition of the SSU Processome to pre-40S (Fig. S1). The
116 current SSU Processome structures all contain rRNA cleaved at A0 but not at A1, indicating that
117 A0 cleavage alone is not sufficient to trigger progression from the SSU Processome [15–17,19].
118 Around the time of Dhr1 function, cleavages at sites A1 within 5' ETS and A2 within ITS1 occur
119 [29,34,35]. It is possible that cleavage at site A1 sets the transition in motion. Site A1 is cleaved
120 by the PIN domain nuclease Utp24 [36–38]. However, it is positioned about 50 Å away from site
121 A1 in the complete SSU Processome [15,16] indicating that some structural rearrangements must
122 occur for it to access its substrate. It is proposed that the essential GTPase Bms1 acts as a
123 molecular switch to drive such structural rearrangements [16], but what signals Bms1 activation
124 is not known. Subsequent cleavage at site A2 separates the SSU precursor from the LSU
125 precursor. When cleavage at site A2 is inhibited, cleavage at the downstream site A3 instead
126 bifurcates the two maturation pathways.

127 Bud23 is a methyltransferase that acts with its cofactor Trm112 to modify guanosine 1575
128 (G1575) within the 3' major domain of 18S rRNA [39–42]. *BUD23* is a nonessential gene in yeast,
129 but its deletion (*bud23*Δ) causes a significant growth defect that correlates with an approximate
130 70% reduction of 40S subunits [39]. Catalytically inactive *bud23* mutants fully complement the

131 growth defect of *bud23*Δ cells suggesting that the presence of the protein but not its
132 methyltransferase activity is needed for ribosome assembly [39,40,43]. Bud23 is not a stable
133 component of the complete SSU Processome and is usually thought to act on a nuclear pre-40S
134 intermediate. Consistent with this notion, the human orthologs of Bud23 and Trm112 were
135 resolved in an early pre-40S structure [44]. Moreover, its binding site is occupied by the assembly
136 factor Emg1 in the SSU Processome structures, precluding Bud23 from assembling into this
137 structure [15–17]. Despite these observations, there are multiple lines of evidence indicating that
138 Bud23 joins the SSU assembly pathway during the transition of the SSU Processome to pre-40S.
139 First, Bud23 coimmunoprecipitates with the late-acting SSU Processome factors Dhr1, Utp14, and
140 Utp2 [45,46], and Trm112 copurifies several late SSU Processome factors including Dhr1 and
141 Utp14 [42]. Second, Bud23 and Trm112 sediment at the positions of both 90S and 40S in sucrose
142 density gradients, reflecting their association with the SSU Processome and pre-40S, respectively
143 [40,42,46]. Third, *bud23*Δ cells are defective in A2 site cleavage [45] which releases the pre-40S
144 particle. Finally, the growth and A2 site cleavage defects caused by the absence of Bud23 are
145 suppressed by extragenic mutations in the SSU Processome factors *DHR1*, *UTP14*, *UTP2 (NOP14)*,
146 and *IMP4* [30,45–47] suggesting that Bud23 acts concurrently with these factors. Despite the
147 evidence that Bud23 enters the 40S biogenesis pathway during the transition of the SSU
148 Processome to pre-40S, the specific function for Bud23 has not been described.

149 Here, we have carried out a comprehensive genetic analysis of extragenic suppressor
150 mutations of *bud23*Δ and identified a genetic and physical interaction network that connects
151 Bud23 to the transition of the SSU Processome to the pre-40S. We found novel extragenic
152 mutations in *IMP4*, *RPS28A*, *UTP2*, *UTP14*, *DHR1*, and *BMS1* that acted as bypass suppressors of

153 *bud23*Δ. Recent SSU Processome structures provide the context to rationalize how these bypass
154 suppressors disrupt SSU Processome structure and suggest a role for Bud23 in the SSU
155 Processome transition. Bms1, Imp4, and Utp2 all interact with the 3' basal subdomain and have
156 helical extensions that embrace the U3-18S substrate of Dhr1. We found that many of the
157 mutations destabilized protein-protein or protein-RNA interactions connecting the 3' major
158 domain to the U3-18S heteroduplexes. Finally, mass spectrometric and Northern blot analysis of
159 particles isolated in the absence of Bud23 revealed an enrichment of late SSU Processome factors
160 and rRNA species not yet cleaved at sites A1 and A2. Together, our data imply that Bud23 binding
161 induces the disassembly of SSU Processome factors connecting the 3' basal subdomain to the U3-
162 18S duplexes. We propose that Bud23 promotes the function of Bms1 and Dhr1 to drive
163 rearrangements for compaction of the 3' basal subdomain in the pre-40S subunit.
164

165 ## Results

166 **Extragenic suppressors of *bud23*Δ map to SSU Processome factors and connect Bud23**
167 **to the U3 snoRNA.** Bud23 methylates G1575 in the 3' basal subdomain of the 18S rRNA [39,40],
168 a region comprised of helices 28, 29, 30 41, 41es10, 42, and 43 (Figs. 1A, 1B, & S2) [17]. The
169 deletion of *BUD23* severely impairs 40S production and cell growth, yet a catalytically inactive
170 Bud23 fully complements *bud23*Δ [39,40], suggesting that 40S assembly requires Bud23 binding
171 but not rRNA methylation. The slow growth defect of *bud23*Δ places strong selective pressure on
172 cells for extragenic bypass suppressors. Our lab previously reported suppressing mutations in
173 *DHR1*, *UTP14*, and *UTP2,* all coding for late acting SSU Processome factors [30,45,46]. We also
174 found mutations in *IMP4* encoding an early SSU Processome factor [47]. These results connected

175 Bud23 to the late events of the SSU Processome, but they did not allow us to rationalize a
176 mechanism for Bud23 function. The complete SSU Processome harbors nearly 70 ribosomal
177 proteins and biogenesis factors, and we postulated that mapping the mutations to current high-
178 resolution structures of the SSU Processome would help illuminate the function of Bud23. To
179 expand the coverage, we screened for additional spontaneous suppressors by continuously
180 passaging cultures of *bud23*Δ until they arose. We then amplified and sequenced the *IMP4*,
181 *DHR1*, *UTP14*, and *UTP2* loci from these suppressed strains, and identified additional mutations
182 in these genes. Suppressed strains that did not contain mutations in these genes were subjected
183 to whole-genome sequencing and genome variant analysis. This revealed novel suppressing
184 mutations in *RPS28A*, a ribosomal protein that binds the 3' basal subdomain, and *BMS1*, an
185 essential GTPase of the SSU Processome. Mutations in *RPS28A* and *BMS1* were confirmed by
186 Sanger sequencing and verified as suppressors of *bud23*Δ after reintroducing the mutations into
187 *bud23*Δ cells (data not shown).

188 Portions of Bms1, Imp4, Rps28, Utp2, and Utp14, but not Dhr1, have been resolved in
189 structures of the SSU Processome [15–17]. Remarkably, Bms1, Imp4, Rps28, and Utp2 all interact
190 directly with the 3' basal subdomain containing the Bud23 binding site (Fig. 1C). These factors
191 appear to contribute to the structural stability of the SSU Processome and form multiple protein-
192 protein and protein-RNA contacts (Fig. 1D). Additionally, Bms1, Imp4, and Utp2 each contain
193 extended alpha-helices that penetrate into the core of the SSU Processome where they embrace
194 the U3 Box A and Box A'-18S duplexes (Fig. 1D). Although Dhr1 is not resolved in any of the SSU
195 Processome structures published to date, we previously mapped its binding site on U3 to the 5'-
196 hinge and Box A, immediately upstream of and overlapping the Box A and Box A'-18S duplexes

197 that we identified as the substrate for Dhr1 unwinding (Fig. S3A) [29]. Only a few segments of
198 Utp14 are resolved in current SSU Processome structures, but Utp14 can be seen binding to pre-
199 rRNA and U3 snoRNA immediately upstream of the duplexes Dhr1 unwinds (Fig. S3A) [15,33].
200 Intriguingly, Utp14 and the factors positioned at the 3' basal subdomain bookend the U3-18S
201 heteroduplexes. Thus, Imp4, Utp2, and Bms1 provide a physical linkage between the 3' basal
202 subdomain and the U3-18S heteroduplexes that are unwound by Dhr1.

203 We identified five novel mutations in *BMS1* and one in *RPS28A* as spontaneous
204 suppressors of *bud23*Δ (Fig. 1E & Supplemental File 1). We also found an additional 15 mutations
205 in *DHR1*, 13 mutations in *IMP4*, two mutations in *UTP14*, and one mutation in *UTP2* that were
206 not isolated in our previous studies. Five additional mutations were identified in *UTP2* using
207 error-prone PCR mutagenesis (discussed below). These observations revealed a network of SSU
208 Processome factors that genetically interact with Bud23 and make multiple physical contacts
209 amongst one another (Fig. 1F). Importantly, this interaction network physically connects the 3'
210 basal subdomain with the U3-18S heteroduplex substrates of Dhr1, suggesting a functional
211 linkage between these two sites. Many of the mutations that we report here and previously [30]
212 are in protein-RNA or protein-protein interfaces where they would appear to weaken
213 interactions within the SSU Processome. Because these mutations bypass the absence of Bud23,
214 we propose that Bud23 binding to the 3' basal subdomain induces the release of factors from
215 this region to promote progression of the SSU Processome to a pre-40S particle. In the following
216 sections, we consider how the *bud23*Δ bypass suppressor mutations affect the dynamics of the
217 particle.

218

219 **The Imp4 and Rps28A mutations mainly cluster around their interfaces with the 3' basal**
220 **subdomain.** We identified 21 unique mutations in *IMP4* and a single mutation within *RPS28A*
221 that suppressed *bud23*Δ (Fig. 1E). All of these mutations partially restored growth in a *bud23*Δ
222 mutant (Fig. 2A), although the *rps28A-G24D* mutation did not suppress as well as the *imp4*
223 mutations, perhaps because expression of the wild-type paralog *RPS28B* partially masked its
224 suppression phenotype. Imp4 is a component of the heterotrimeric Mpp10-Imp3-Imp4 sub-
225 complex [48–52] which enters the SSU Processome at an early stage of its assembly, during
226 transcription of the 5' ETS [6,7]. The Mpp10 complex may serve as an initial binding platform for
227 several additional SSU Processome factors [53]. Recent structures show that Imp4 is positioned
228 in the core of the SSU Processome where its N-terminal domain (NTD) contacts the U3-18S
229 heteroduplexes while its RNA-binding Brix domain is cradled in the concave RNA fold of the 3'
230 basal subdomain (Fig. 2B) [15–17]. On the other hand, the ribosomal protein Rps28 binds to the
231 opposite, convex surface of the 3' basal subdomain (Fig. 2B), adjacent to but not occluding the
232 Bud23 binding site (Fig. 2B; marked by G1575) [44].
233 The mutations in Imp4 primarily mapped to two regions of the protein (Fig. 2C). Most of
234 the mutations were in the Brix domain of Imp4 at its interface with the 3' basal subdomain RNA,
235 henceforth "rRNA interaction" mutations (Fig. 2C). These included mutations of residues S93,
236 R94, S101, R116, N118, N121, and R146 which are all expected to form hydrogen bonds with the
237 rRNA [15,16]. These mutations likely weaken the affinity of the protein for the rRNA. The single
238 Rps28-G24D mutation maps to its rRNA interface with the 3' basal subdomain. Unlike Imp4,
239 Rps28 is an integral component of the small subunit and remains associated with the mature
240 ribosome. Consequently, it is unlikely that the glycine to aspartate substitution promotes release

241 of Rps28. More likely, this mutation may increase the flexibility of the RNA to facilitate release of
242 Imp4 (Fig. 2C). Five of the mutations in Imp4, in residues D74, Y77, H156, H159 and H208, mapped
243 to an intramolecular domain interface between the core of the protein and the NTD that interacts
244 with the U3 Box A'-18S duplex, henceforth "NTD interaction" mutations (Fig. 2D). The NTD
245 interaction mutations may alter the flexibility of the NTD, thereby destabilizing its interaction
246 with the U3 Box A'-18S duplex. The observation that *imp4* mutations that suppress *bud23*Δ are
247 predicted to weaken the affinity of Imp4 for the 3' basal subdomain, suggests that Bud23 binding
248 to the 3' basal subdomain leads to disruption of the protein-RNA interactions in this region.

249 Bud23 is needed for efficient processing at the A2 cleavage site [39]. To ask if the
250 suppressing mutations in *IMP4* and *RPS28A* bypass this rRNA processing defect in *bud23*Δ cells,
251 we prepared total RNA from actively dividing wild-type (WT) cells or *bud23*Δ cells with or without
252 a suppressing mutation in *IMP4* or *RPS28A* and probed for rRNA processing intermediates by
253 Northern blotting (Fig. 2E). As we reported previously [45], *bud23*Δ cells showed a loss of the
254 27SA2 rRNA intermediate, indicating loss of A2 cleavage, and reduced levels of 18S rRNA
255 compared to WT cells, but no concurrent accumulation of 23S rRNAs. Suppression of *bud23*Δ by
256 the *imp4* and *rps28A* mutants partially restored levels of the 27SA2 rRNA intermediate and 18S
257 rRNA indicating a restoration of cleavage at site A2 and 40S biogenesis. Surprisingly, *bud23*Δ cells
258 also slightly accumulated the 22/21S intermediates (Fig. 2E). 22S represents rRNA cleaved at sites
259 A0 and A3 but not A1 or A2 while 21S represents rRNA cleaved at sites A1 and A3 but not A2.
260 (Fig. S1). Although the A2-A3 probe cannot distinguish between the 22S and 21S intermediates
261 the A0-A1 probe gave a similar hybridization signal indicating that the 22S rRNA accounts for
262 some of this signal (Fig. 2E). Suppression of *bud23*Δ partially alleviated the accumulation of this

263 species. This was most evident in the strains harboring the *imp4* mutants S93T, R94S, N121I, and
264 H159R. These data indicate that Bud23 affects not only A2 processing, as we previously reported
265 [39], but also cleavage at A1.

266 As a complementary approach to ask if *bud23*Δ suppressors restored 40S biogenesis, we
267 analyzed ribosomal subunit levels on sucrose density gradients after separating free ribosomal
268 subunits, 80S, and polysomes from wild-type cells and *bud23*Δ cells with or without a suppressing
269 mutation. In wild-type cells, there was an appreciable steady-state level of free 40S and 60S
270 subunits (Fig. 2F). In contrast, in *bud23*Δ cells in which 40S production is limited, the free 40S
271 peak disappeared and the amount of free 60S was dramatically increased, at the expense of 80S
272 (Fig. 2F). The introduction of suppressing mutations in *imp4* or *rps28a* partially restored the levels
273 80S and free 40S, similar to the suppression of *bud23*Δ by mutations in *utp14* or *utp2* that we
274 reported previously [45]. Taken together, the Northern blotting and sucrose density gradient
275 data indicate that *imp4* and *rps28A* mutants partially alleviate the 40S biogenesis defects of
276 *bud23*Δ cells.

277

278 **Utp2 mutants that suppress *bud23*Δ destabilize Utp2 interaction with Imp4.** Our lab
279 previously identified *utp2-A2D* as a spontaneous and dominant suppressor of *bud23*Δ that
280 partially restores 40S biogenesis and A2 processing of the primary rRNA transcript [45]. From our
281 screen for additional spontaneous suppressors of *bud23*Δ, we found an additional Utp2
282 mutation, *utp2-L9S*, that suppressed *bud23*Δ (Fig. 3A). Utp2, also known as Nop14, assembles
283 into the SSU Processome with its binding partners Emg1, Noc4, and Utp14 [54–56], once the 3'
284 minor domain is fully transcribed [6,7]. The association of human Utp2 with human pre-40S

285 complexes indicates that Utp2 remains on nascent particles during the transition from the SSU
286 Processome to pre-40S [44] suggesting that it has an active role in particle progression.

287 To gain further insight into the mechanism by which mutations in *UTP2* suppress *bud23*Δ,
288 we performed random PCR mutagenesis of *UTP2* and identified six additional mutations in *UTP2*
289 that suppressed *bud23*Δ to different degrees (Fig. 3B; left panel). In this screen we also reisolated
290 the previously identified *utp2-A2D* mutation. All mutants fully complemented loss of Utp2 (Fig.
291 3B; right panel). The suppressing mutations all mapped to the N-terminal domain of Utp2; four
292 clustered around the extreme N-terminus and another three clustered around residues 148-151.
293 In an attempt to generate mutants with stronger phenotypes than the individual mutants, we
294 generated the combinatorial mutants *utp2-DPE* containing the mutations A2D, L6P, and K7E, and
295 *utp2-SSH* harboring the mutations L148S, F149S, and L151H. Both of the combinatorial mutants
296 retained the ability to suppress *bud23*Δ and fully complemented loss of *UTP2*, but *utp2-SSH* was
297 a stronger suppressor than *utp2-DPE* (Fig. 3B).

298 Based on recent partial structures of Utp2 within the SSU Processome [15,16] the globular
299 domain of Utp2 directly contacts the Emg1 heterodimer, Enp1, and Noc4 within a region of the
300 3' major domain that will make up the beak of the mature SSU, while its extended N- and C-
301 terminal arms pierce deep into the core of the SSU Processome. The C-terminal arm of Utp2
302 contacts the U3 Box A'-18S duplex while its NTD contacts the Brix domain of Imp4 (Figs. 1D & 3C).
303 Notably, four of the residues (L6, K7, L9 and F58) mutated in our screen were resolved in current
304 structures of the SSU Processome (Fig. 3C). Residues L6, K7, and L9 are within a small helix on the
305 extreme N-terminus of Utp2 that interacts with Imp4, while K7 also appears to contact the
306 phosphate backbone of C1623 of the 3' basal subdomain. Meanwhile, F58 of Utp2 makes an

307 additional nearby contact between these proteins. These observations prompted us to speculate
308 that the *utp2* suppressors of *bud23*Δ perturb the interaction between Utp2 and Imp4. Previous
309 large-scale yeast-two hybrid (Y2H) studies did not report an interaction between Utp2 and Imp4
310 [54,55]. However, those studies used Utp2 constructs harboring N-terminal fusions of GAL4
311 activating or DNA binding domain (AD and BD, respectively). Because the apparent interaction
312 between Utp2 and Imp4 requires the extreme N-terminus of Utp2 (Fig. 3C), such a fusion protein
313 could sterically hinder their interaction. To this end, we cloned a Utp2 Y2H construct harboring
314 an HA-tagged GAL4 activating domain fused to its C-terminus (Utp2-AD-HA), which allowed us to
315 detect an interaction between Utp2-AD-HA and BD-myc-Imp4 (Fig. 3D; left panel). Using this
316 system, we assayed the Utp2-DPE, Utp2-F58S, and Utp2-SSH mutants for their ability to interact
317 with Imp4. All of the mutants showed decreased interaction with Imp4 with the Utp2-F58S and
318 Utp2-SSH mutants being the most severe. All the mutant Utp2 proteins were expressed to similar
319 levels indicating that the reduced interaction was not due to differences in expression or
320 degradation of the mutant proteins (Fig. 3D; right panel). The results from the analysis of Utp2-
321 DPE and Utp2-F58S are consistent with the notion that the mutations in Utp2 that suppress
322 *bud23*Δ disrupt the interaction between Utp2 and Imp4. The result of Utp2-SSH losing interaction
323 with BD-Imp4 suggests that the flexible, unresolved region of Utp2 between R116 and P201
324 interacts with Imp4, but we cannot rule out the formal possibility that these mutations suppress
325 *bud23*Δ by some other means.

326 F58 of Utp2 fits into a hydrophobic pocket of Imp4 (Fig. 3E; upper panel). Interestingly,
327 two mutations in *IMP4*, V170F and P252L, that suppressed *bud23*Δ (Figs. 2A & 2B) map to
328 residues that line this pocket (Fig. 3E; lower panel). The positions of these two mutations predict

329 that they could also disrupt the interaction between Imp4 and Utp2. To test this possibility, we
330 introduced the V170F and P252L mutations into the BD-myc-Imp4 vector and assayed for their
331 interaction with Utp2-AD-HA. Indeed, mutation of either of these residues caused a loss of
332 interaction between Utp2 and Imp4 (Fig. 3F; upper panel), and the loss of interaction could not
333 be explained by reduced protein expression of the mutant Imp4 constructs (Fig. 3F; lower panel).
334 These results, together with the Y2H assays using mutant Utp2 strongly suggest that disrupting
335 the interaction between Imp4 and Utp2 bypasses the 40S assembly defect in the absence of
336 Bud23.
337
338 **Bms1 mutants that suppress *bud23*Δ are poised to affect the conformational state of Bms1.**
339 We found five *bud23*Δ-suppressing mutations within *BMS1* (Figs. 1F & 4A). Like the mutations in
340 *DHR1*, *UTP14*, *UTP2*, *IMP4*, and *RPS28A* (Fig. 2E) [30,45,46], mutant *bms1* alleles partially
341 alleviated the rRNA processing defects and restored 40S biogenesis (Figs. 4B & 4C) suggesting
342 that these mutations overcome the same biogenesis defect in the absence of Bud23 that the
343 other *bud23*Δ suppressors do. *BMS1* encodes a 136 kDa GTPase that is essential for 40S
344 biogenesis [57,58]. Bms1 forms a subcomplex with Rcl1 [58–61] prior to its entry into the SSU
345 Processome after completion of the 3' minor domain [6,7]. The GTPase activity of Bms1 has been
346 confirmed *in vitro* [59,60], and its ability to bind GTP is essential [61] suggesting that it is a
347 functional GTPase *in vivo*. However, the specific role of Bms1 within the SSU Processome has not
348 been well explored. GTPases often serve as molecular switches that undergo conformational
349 changes (reviewed in [62]). Due to its position in the SSU Processome, it has been suggested that
350 Bms1 helps remodel the SSU Processome core so the endonuclease Utp24 can access and cleave

351 the A1 site [16]. Thus, this model predicts that Bms1 has a role in the progression of the SSU
352 Processome to the pre-40S.

353 More than half of Bms1 has been resolved in structures of the SSU Processome and can be
354 divided into five major domains and two small regions that bind its partner Rcl1 and the
355 acetyltransferase Kre33 (Fig. 4D) [15–17]. Domain I contains the GTPase catalytic site and,
356 together with the beta-barrels of domains II and III, forms a globular body. Domain IV protrudes
357 from this globular body to interact with the 3' basal subdomain RNA and contacts the CTDs of
358 Imp4 and Utp2 (Fig. 4E). Finally, the C-terminal domain V begins as an extended strand that lays
359 on domain III before becoming an extended alpha-helix that inserts between the U3 Box A'-18S
360 and U3 Box A-18S heteroduplexes (Fig. 4D). Although the five mutations that suppressed *bud23*Δ
361 map to domains I, II, III and V (Fig. 4D; upper panel) , in 3D structure the mutated residues D124,
362 D843, A903, and S1020 lie immediately under the unstructured strand connecting domain IV to
363 the extended C-terminus (Fig. 4F). Thus, four of the five suppressing mutations likely promote
364 the flexibility of this connecting loop. G813 is located in the connector between Domains II and
365 III where it could alter the relative positioning of these two domains and influence how domain
366 III interacts with the unstructured strand of domain V.

367 Bms1 is structurally related to the translation elongation factor EF-Tu which delivers amino-
368 acyl tRNAs to the ribosome (Fig. S4A) [57]. Comparison of the Bms1 structure from the SSU
369 Processome to the crystal structures of EF-Tu bound to GDP or the non-hydrolysable GTP analog,
370 GDPNP, suggests that Bms1 is in the GTP-bound state in the SSU Processome structures and
371 allows us to speculate how Bms1 functions. The beta-barrels of domains II and III of Bms1 are
372 conserved in EF-Tu (Fig. S4B). In the GTP-bound state, the beta-barrels of EF-Tu are positioned to

373 accommodate tRNA binding (Fig. S4C) [63]. In GDP-bound EF-Tu the beta-barrels are rotated to
374 promote tRNA release (Figs. S4C & S4D) [64]. Interestingly, the comparison of the EF-Tu and Bms1
375 structures revealed that the space occupied by tRNA in EF-Tu (Fig. S4E) is occupied by an N-
376 terminal helix of Mpp10 and the unstructured strand of Bms1 that connects domain IV to the
377 extended C-terminus that interacts with U3 (Fig. S4F). This observation suggests that the GTP
378 hydrolysis-induced conformational changes of Bms1 could facilitate undocking of the
379 unstructured strand of Bms1 and Mpp10 from the conserved core of Bms1. Notably, four of the
380 five mutations in *BMS1* that suppressed *bud23*Δ were either within or contact this strand of Bms1
381 (Fig. S4F). We suggest that these mutations facilitate release of this strand and, perhaps, Mpp10
382 from Bms1. As this C-terminal domain has been proposed to regulate the timing of Utp24-
383 calatalyzed cleavage of the A1 site [16], the functional interaction between Bud23 and Bms1 may
384 explain why *bud23*Δ cells were deficient in A1 site cleavage (Figs. 2E & 4B), however we cannot
385 exclude the possibility that this defect is indirect. Future molecular analysis is needed to better
386 characterize the role of Bms1 in SSU Processome disassembly.
387
388 **Disruption of Dhr1 and Utp14 interaction suppresses *bud23*Δ.** Our lab previously reported
389 10 mutations in *DHR1* that suppress *bud23*Δ [46]. Here, we isolated an additional 15 suppressing
390 mutations within *DHR1* (Figs. 1F & 5A). Dhr1 is the DEAH-box RNA helicase responsible for
391 unwinding the U3 snoRNA from the SSU Processome [29,34]. The protein harbors a conserved
392 helicase core containing two RecA domains, a Winged-helix (WH) domain, a Helical Bundle (HB)
393 domain, and an OB-fold domain (Fig. 5A). Dhr1 also contains an N-terminal domain (NTD) that
394 interacts with Bud23 [40,46] and a unique C-terminal domain (CTD) that enhances its interaction

395 with its activator Utp14 [30–32]. Although Dhr1 has yet to be resolved in SSU Processome
396 structures, recent crystal structures of recombinant yeast Dhr1 [31] and its murine homolog
397 DHX37 [32] lacking the NTD allow us to map most of the mutated residues to structure (Fig. 5B).
398 Consistent with our previous report [46], the overwhelming majority of the mutations map to
399 residues on the surface of the RecA1 and RecA2 domains (Fig. 5C). We previously reported that
400 Utp14, the cofactor of Dhr1, binds the RecA1/2 domains [30]. Based on this, we hypothesized
401 that the mutations within the RecA1/2 domains could affect its interaction with Utp14. To this
402 end, we again turned to yeast 2-hybrid analysis between BD-myc-Dhr1 and AD-HA-Utp14. We
403 made three Dhr1 Y2H constructs that combined several mutations within or proximal to the
404 RecA1 domain (E360K, E397D, E402G, D408Y), within the RecA2 domain (H593Y, R596C, E831K),
405 or in both the RecA1 and RecA2 domains (R563M, D566Y, E831K, F837L) and tested them for the
406 ability to interact with Utp14. All three mutants showed a significant loss of interaction with
407 Utp14 (Fig. 5D; left). All three of the mutant proteins expressed similarly (Fig. 5D; right), indicating
408 that the loss-of-interaction was not due to differential expression. Thus, we conclude that
409 mutations within the RecA1 and RecA2 of Dhr1 that bypass *bud23*Δ do so by weakening its
410 interaction with Utp14. Several mutations mapped to the interface between the two RecA
411 domains while glutamate 1037, which is mutated to lysine or glutamine in two of the mutants,
412 coordinates residues important for RNA binding. Although additional *in vitro* analysis is required
413 to understand how these mutations impact Dhr1 function, Dhr1-E1037K,Q likely impairs RNA
414 binding.

415 Utp14 stimulates the unwinding activity of Dhr1 [30,32,65]. We previously reported five
416 mutations within Utp14 that suppress the growth defect of *bud23*Δ [30]. Notably, these

417 mutations are within an unresolved region of Utp14 spanning residues 719 to 780 that interacts
418 with Dhr1 (Fig. S3A & S3B), and extensive mutation or deletion of this region reduced Utp14
419 interaction with Dhr1, Utp14-dependent activation of Dhr1 unwinding activity *in vitro* and
420 phenocopied catalytically null Dhr1 *in vivo* [30]. Here, we report two additional mutations in
421 Utp14, W791L and W794L, that suppressed *bud23*Δ (Fig. S3B). These mutations are slightly
422 downstream of those previously identified and affect two highly conserved tryptophan residues
423 in a motif weakly reminiscent of a G patch, a motif common to activators of DEAH/RHA RNA
424 helicases [30]. Determining how the mutations in Dhr1 and Utp14 bypass loss of Bud23 will
425 require further work. However, the majority of the mutations in Dhr1 and Utp14 are predicted
426 to diminish their interaction and consequentially reduce the activity of Dhr1 (Fig. 5) [30]. Thus,
427 the simplest interpretation is that the bypass of *bud23*Δ by Dhr1 and Utp14 mutants is
428 accomplished by reducing the activity of Dhr1, possibly providing increased opportunity for the
429 helicase to work on a suboptimal substrate (see Discussion).
430
431 **Depletion of Bud23 partially inhibits SSU Processome progression.** The above genetic
432 results suggest that disrupting protein-protein and protein-RNA interactions in the 3' basal
433 subdomain of the SSU Processome can partially bypass the absence of Bud23. We interpret these
434 results to indicate that Bud23 binding leads to disassembly events that promote the remodeling
435 of this region the SSU Processome. To test the idea that Bud23 promotes disassembly events, we
436 characterized pre-ribosomal particles in the absence of Bud23. We introduced a genomically
437 encoded C-terminal Auxin-Induced Degron (AID) tag on Bud23 for rapid depletion of Bud23 upon
438 the addition of the small molecule auxin without the need for shifting carbon sources [66]. The

439 *BUD23-AID* strain grew similar to wild-type cells on media lacking auxin, while it showed a growth
440 defect comparable to the *bud23*Δ strain on media containing auxin indicating that the AID tag is
441 functional and does not significantly impact Bud23 function (Fig. 6A). Bud23-AID was significantly
442 depleted after 10 minutes and was undetectable after two hours of auxin treatment (Fig. 6B).

443 We first asked if Bud23 depletion impacted the association of Imp4 with pre-ribosomes.
444 We depleted Bud23-AID for two hours and separated particles by ultracentrifugation on sucrose
445 density gradients and fractionation. We then isolated the proteins from each fraction and
446 performed western blot analysis for Imp4. In the presence of Bud23, Imp4 sedimented
447 throughout the gradient with enrichment in the 40S to 80S fractions and near the top of the
448 gradient (Fig. 6C). The Imp4 in fractions 2 and 3 likely reflects its association with the Mpp10 sub-
449 complex [48,51,67] whereas the Imp4 in the 80S region reflects its association with the SSU
450 Processome at 90S. We also monitored the sedimentation of the biogenesis factor Enp1
451 harboring a C-terminal Tandem Affinity Purification (TAP) tag which also sedimented throughout
452 the gradient indicating its binding to both the SSU Processome and pre-40S particles [20]. In the
453 absence of Bud23-AID, both Imp4 and Enp1-TAP showed reduced sedimentation in the 80S
454 region but increased or maintained sedimentation in the 40S region of the gradient. The
455 enrichment of these proteins in fractions 6 and 7 in the absence of Bud23 is reminiscent of the
456 ~45S intermediate that accumulates in catalytically deficient Dhr1 mutants and are thought to
457 represent a partially disassembled SSU Processome [29,30,46]. These results suggest that Imp4
458 and Enp1 are retained on a partially disassembled SSU Processome in the absence of Bud23,
459 however we cannot exclude the possibility that the altered their sedimentation is due to
460 degradation of unstable SSU Processome particles.

461 To further understand the nature of the 40S precursors that accumulate in the absence
462 of Bud23, we affinity purified Enp1-TAP particles from WT and Bud23-AID strains after two hours
463 of auxin treatment. Enp1-TAP is an ideal bait for these experiments as it binds to pre-ribosomes
464 before Bud23 binding and is released after Bud23 function [20], and because its sucrose density
465 gradient sedimentation was influenced by Bud23 (Fig. 6C). Following enzymatic elution, the
466 particles associated with Enp1 were sedimented through sucrose cushions to separate them from
467 any extraribosomal Enp1. The associated proteins were then separated by SDS-PAGE and
468 analyzed by Coomassie staining. The depletion of Bud23 led to both the reduction of and
469 accumulation of multiple protein species (Fig. 7A; black lines and blue lines, respectively). Mass
470 spectrometry of these discrete species identified the depleted proteins as the pre-40S factors
471 Tsr1, Rio2, and Nob1, while mostly late-acting, SSU Processome factors comprised the
472 accumulated factors suggesting that the loss of Bud23 precluded their release from pre-
473 ribosomes.

474 To further characterize the purified particles, we used mass spectrometry to analyze the
475 entire proteomic compositions of the wild-type and Bud23-depleted particles. To approximate
476 stoichiometry for each 40S assembly protein, we calculated its relative spectral abundance factor
477 (RSAF) by dividing the spectral counts for each protein by its molecular weight then normalizing
478 this value to the bait, Enp1 (Fig. S5 & Supplemental File 2). This analysis showed various proteins
479 that were accumulated or depleted from these particles. Interestingly, the proteins that showed
480 genetic interaction with *bud23*Δ remained relatively constant in the absence of Bud23, with the
481 exception of Utp2 which increased in abundance. As Enp1 and Imp4 co-sedimented in the
482 absence of Bud23 (Fig. 6C), we interpret this observation to indicate that these particles are

483 arrested upstream of the release of these factors where they remain stoichiometric with Enp1.
484 To simplify our analysis, we calculated a log2-fold change between Bud23-depleted and wild-type
485 particles for each protein and considered a result significant if a protein showed a ± 0.5-fold
486 change with a difference of at least 10 spectral counts (Fig. S6). This analysis revealed a set of 26
487 proteins that altered upon Bud23-depletion. These results agreed with what we observed by SDS-
488 PAGE in Fig. 7A in that there was an accumulation of mainly SSU Processome factors and a
489 depletion of mostly pre-40S factors. Notably, Noc4, Utp2, and Rrp12 bind to the 3' major domain
490 [15–17,19] while several factors, such as Bfr2, Enp2, Lcp5, Kre33, and Mrd1 have roles in the final
491 assembly of the SSU Processome [19,68]. Strikingly, the pre-40S factors Slx9 and Rio1 [69–71]
492 also accumulated in the absence of Bud23. These results suggest that without Bud23 the SSU
493 Processome improperly disassembles in that certain regions are progressed to a pre-40S-like
494 state whereas other regions appear arrested.

495 We also probed for the rRNA intermediates that co-precipitated with Enp1-TAP in the
496 presence and absence of Bud23 (Fig. 7B). We observed that Enp1 decreased association with the
497 23S rRNA with a concomitant accumulation of both 21S and 22S RNAs in the absence of Bud23.
498 By quantifying the amount of 22S relative to 35S detected with A0-A1 probe vs the amount of
499 21S/22S relative to 35S detected with the A2-A3 probe we calculate that the 21S and 22S species
500 are approximately equally abundant in the Enp1-TAP sample from Bud23-depleted cells. The
501 accumulation of 21S and 22S indicates that processing at A2 was inhibited upon Bud23 depletion,
502 as we have previously reported [39]. The accumulation of 22S was unexpected as this indicates a
503 defect in A1 cleavage as well. Furthermore, we saw a modest accumulation of the A0-cleaved 5'
504 ETS rRNA (~1.5-fold) and U3 snoRNA (~1.2-fold). Consistent with what is seen in whole cell

505 extracts of *bud23*Δ cells (Figs. 2E & 4B) [45,46], we also saw that 27SA2 intermediate was present
506 in the input and IP for the wild-type sample, but totally absent in the Bud23-depleted sample
507 (Fig. 7B). These results reconfirm that Bud23 is needed for efficient processing at A2 and support
508 the possibility that Bud23 also impacts cleavage at A1.

509 **Discussion**

510 Bud23 was identified as the methyltransferase that modifies G1575 in 18S rRNA and is
511 thought to act at a relatively late stage of small subunit assembly in the nucleolus [39,42].
512 Although it is conserved from yeast to humans [40,72–74] and deletion of *BUD23* in yeast leads
513 to severely impaired growth [39], its methyltransferase activity is dispensable for ribosome
514 assembly [39,72]. This indicates that the primary function of Bud23 stems from its binding to SSU
515 precursors, however the role of Bud23 in small subunit assembly is not well understood. Bud23
516 and its cofactor Trm112 co-sediment with both the pre-40S and the SSU Processome
517 [40,42,45,46]. Consistent with this, Bud23 also co-purifies with late-acting Processome factors
518 and early pre-40S factors [45,46]. Although Bud23 is not a component of the SSU Processome, as
519 highlighted by the fact that its binding site is occupied by the assembly factor Emg1 in the SSU
520 Processome structures [15–17], our work strongly implicates Bud23 in the disassembly of the SSU
521 Processome as it transitions to a pre-40S. The absence of Bud23 impairs A2 site cleavage [39], an
522 event that is tied to the transition. Prior to A2 cleavage, the U3 snoRNA is unwound from the 18S
523 rRNA which is catalyzed by the RNA helicase Dhr1 and its co-factor Utp14 [29,30]. Dhr1 physically
524 interacts with Bud23 [40,46], and we previously reported that mutations in Dhr1, Utp14, or other
525 SSU Processome factors suppress the growth and A2 site cleavage defects in *bud23*Δ cells [30,45–
526 47]. These results indicate that Bud23 enters the maturing SSU assembly pathway as the SSU

527 Processome transitions to the pre-40S. Here, we provide a significant body of additional evidence
528 to build a case for the role of Bud23 in this transition.
529
530 **Does Bud23 promote the compaction of SSU structure?** The 3' basal subdomain forms a
531 compact RNA unit whose structure remains relatively unchanged between the SSU Processome
532 and Bud23-bound pre-40S, despite its dramatic repositioning during this transition. The majority
533 of mutations that we found as suppressors of *bud23*Δ were in *IMP4* and *DHR1* with additional
534 mutations in *BMS1*, *RPS28A*, *UTP2*, and *UTP14* (Fig. 1D & 1E). Imp4, Rps28, Utp2 and Bms1 all
535 interact with the 3' basal subdomain of 18S rRNA. The Imp4 mutations clustered primarily in its
536 interface with the RNA of the 3' basal subdomain (Fig. 2C), opposite the binding site of Bud23
537 and are predicted to be disrupting interactions. The Brix domain of Imp4 also contacts the NTD
538 of Utp2 (Fig. 3C), and we showed that suppressing mutations on either side of this interface
539 disrupted their interaction (Figs. 3D & 3F). Likewise, the mutations in the GTPase Bms1 are
540 expected to affect intramolecular interactions in a manner that promotes a conformational
541 change within Bms1 (Fig. 4F). As Bms1 simultaneously binds to the 5' domain and the 3' basal
542 subdomain, a conformational change could induce large-scale repositioning of RNA elements
543 within the SSU Processome. The picture that emerges is that the *bud23*Δ suppressing mutations
544 define a network of protein-protein and protein-RNA contacts that stabilize the 3' basal
545 subdomain within the SSU Processome structure. Disrupting this interaction network bypasses
546 the requirement for Bud23, suggesting that the function of Bud23 is to destabilize these
547 interactions to promote progression to the pre-40S. Consistent with this idea, pre-ribosomal
548 particles accumulated late-acting SSU Processome factors in the absence of Bud23 (Figs. 7A &

549 S6). Thus, we propose that Bud23 binding to the 3' basal subdomain promotes large-scale
550 rearrangements as the open structure of the SSU Processome collapses into the more compact
551 structure of the pre-40S (Fig. 8A).
552
553 **Is Dhr1 unwinding of the U3 snoRNA coordinated with the GTPase activity of Bms1?** The
554 network of genetic and physical interactions that we define in this work functionally link the RNA
555 helicase Dhr1 and the GTPase Bms1. These two enzymes are thought to drive structural
556 rearrangements critical to the transition of the SSU Processome to a pre-40S particle. Dhr1
557 catalyzes U3 snoRNA removal [29] while Bms1 is proposed to remodel structure to promote A1
558 site cleavage [16]. In addition to the functional linkage between Dhr1 and Bms1, the 3' basal
559 subdomain connects directly to the U3-rRNA duplexes that Dhr1 unwinds via long alpha helical
560 extensions of Imp4, Utp2, and Bms1, suggesting that the events at the 3' basal subdomain are
561 coordinated with Dhr1 unwinding U3. The linkage of Dhr1 and Bms1 in the disassembly of the
562 SSU Processome is reminiscent of the relationship between the DExH RNA helicase Brr2 and the
563 EF-G-like GTPase Snu114 that regulate Spliceosome disassembly [75]. In the case of the
564 spliceosome, it is believed that nucleotide-dependent conformational changes in Snu114 activate
565 Brr2, mediated through the C-terminus of Snu114. It is possible that the actions of Dhr1 and Bms1
566 are similarly coordinated. Bms1 has a globular GTPase domain composed of domains I-III that
567 binds helices 15-18 of the 5'-domain of 18S rRNA while domain IV binds to the 3' basal subdomain
568 [15,16]. A long C-terminal helix of Bms1 extends into the SSU Processome core where it wedges
569 between the U3 Boxes A and A' heteroduplexes with 18S rRNA (Figs. 1D & S3A), the substrates
570 of Dhr1. In this way, Bms1 and Dhr1 can be mechanistically linked. We previously mapped the

571 binding site of Dhr1 to U3 snoRNA immediately downstream of the Boxes A and A'
572 heteroduplexes [29]. As Dhr1 is a DEAH-box helicase it likely translocates in a 3' to 5' manner [32]
573 and would be poised to disrupt the U3 heteroduplexes. However, the helical extension of Bms1
574 with those of Utp2 and Imp4 could act as obstructions to control Dhr1 translocation.
575
576 **What is the role of Bud23 in SSU Processome disassembly?** In the mature SSU
577 Processome, Emg1 occupies the Bud23 binding site [15,16]. Thus, the release of Emg1 and
578 possibly additional disassembly events must precede Bud23 recruitment. Consequently, we
579 envision that Bud23 does not act directly on the intact SSU Processome but on a later,
580 intermediate particle during the transition to pre-40S. The genetic linkage of Bud23 to Bms1 and
581 Dhr1 as well as the physical linkage formed by Bms1 between the U3-18S heteroduplexes, that
582 Dhr1 unwinds, and the 3' basal subdomain, where Bud23 binds, suggest that Bud23 may
583 coordinate their activities. We propose a mechanism in which Bud23 binding facilitates SSU
584 Processome progression. After A0 site cleavage but before A1 and A2 site processing Dhr1 binds
585 to the SSU Processome [17,29,31,33–35], and Utp14 positions Dhr1 ahead of the U3-18S
586 heteroduplexes where it is poised for unwinding [30,33]. However, the helical extensions of
587 Bms1, Imp4, and Utp2 embrace and stabilize the U3-18S heteroduplexes thereby inhibiting Dhr1
588 unwinding. (Fig. 8B). After a partial disassembly of the SSU Processome, including the release of
589 Emg1 from the 3' basal subdomain, Bud23 binding signals the GTPase activity of Bms1 to drive
590 structural rearrangements to displace the helical extensions allowing Dhr1 to progress through
591 its substrate.
592

593 **How do the Dhr1 and Utp14 mutants bypass *bud23*Δ?** The activity of Dhr1 is stimulated
594 by interaction with Utp14 both *in vivo* and *in vitro* [30,32,65]. This interaction is mediated by a
595 short loop within Utp14, spanning residues 719-780 in the yeast protein [30], that is conserved
596 from yeast to mammals [30,32,65]. Y2H and *in vitro* experiments show that mutation of this loop
597 reduces the interaction between Utp14 and Dhr1 and decreases stimulation of Dhr1 activity
598 [30,32]. Consistent with the *in vitro* results, mutation of this loop of Utp14 phenocopies a
599 catalytically defective Dhr1 mutant *in vivo* [30]. Single point mutations in this loop were identified
600 as suppressors of *bud23*Δ, suggesting that weakening the interaction between Utp14 and Dhr1
601 and likewise reducing the activation of Dhr1 by Utp14 suppresses *bud23Δ*. Similarly, the majority
602 of the mutations in Dhr1 that suppress *bud23Δ* lay across the surface of the RecA domains (Fig.
603 5C) and combining multiple such mutations leads to reduced interaction with Utp14 (Fig. 5D).
604 The ATPase activity of Dhr1 also depends on its interaction with RNA [29,30,65], and other
605 *bud23*Δ-suppressing mutations, such as *dhr1-E1037K,Q*, affect residues that appear important
606 for RNA binding. As with the Utp14 mutations, it appears that reducing Dhr1 activity leads to
607 bypass of *bud23Δ*. We suggest that in the absence of Bud23, the structural context in which Dhr1
608 unwinds the U3-18S heteroduplexes is altered and wild-type Dhr1 activity promotes discard of a
609 suboptimal substrate. Dhr1 unwinds U3 from the 18S to allows folding of the central pseudoknot
610 [29,65]. If Bud23 promotes rearrangements within the transitioning processome that are
611 necessary for folding of the CPK, then in the absence of Bud23, Dhr1 unwinding may be largely
612 unproductive, acting before substrates are positioned for efficient folding of the central
613 pseudoknot. Mutations in Dhr1, or in Utp14, that reduce its activity, may afford more time for
614 rearrangements within the transitioning SSU Processome to allow productive unwinding by Dhr1.

615 In this model, mutations in factors binding the 3' basal subdomain (Imp4, Bms1, and Utp2) may
616 help overcome the requirement of Bud23 to afford a more favorable substrate for central
617 pseudoknot folding. Similar models of kinetic proofreading have been developed for RNA
618 helicases involved in splicesosomal rearrangements [76] where, for example, mutations in Prp28
619 that reduce its ATPase activity enhance the splicing efficiency of a suboptimal substrate [77].
620

621 ## Materials and methods

622 **Strains, growth media, genetic methods, and yeast two-hybrid (Y2H) analysis.** All S.
623 cerevisiae strains and sources are listed in Table 1. AJY2676 was generated by genomic
624 integration of *Eco*RI-digested pAJ4339 [78] into AJY2161 to replace the *KanMX* marker with
625 *CloNAT*. AJY3156 was generated by genomic integration of *bud23Δ::KanMX* into AJY2665.
626 AJY4175 was generated by transforming pAJ4094 into a *UTP2/utp2Δ::KanMX* heterozygous
627 diploid strain [79], sporulated, and dissected. AJY4395 was generated by genomic integration of
628 *AID-HA::OsTIR1::LEU2* amplified from pJW1662 [80] into the *BUD23* locus of AJY2665. All yeast
629 strains were cultured at 30°C in either YPD (2% peptone, 1% yeast extract, 2% dextrose), YPgal
630 (2% peptone, 1% yeast extract, 1% galactose), or synthetic dropout (SD) medium containing 2%
631 dextrose unless otherwise noted. When appropriate, media were supplemented with 150 to 250
632 µg/ml G418 or 100 µg/ml nourseothricin. All plasmids and sources are listed in Table 2. Y2H
633 analysis was performed as previously described [33].
634

635 **Identification of additional spontaneous suppressors of *bud23*Δ.** AJY2676 cells were
636 inoculated into 200 µL of YPD media in a 48-well format plate. Cells were cultured with

637 continuous shaking until saturation then diluted into fresh media. After each passage, cells were
638 plated onto YPD plates to test for the presence of suppressors. This process was iterated for each
639 culture until suppressors were observed. Single colonies of each suppressor strain were obtained
640 and genomic DNA was prepped using MasturePure™ Yeast DNA Purification Kit (Lucigen). The
641 *DHR1*, *IMP4*, *UTP2*, and *UTP14* loci were amplified and sequenced by Sanger to identify mutations
642 in known suppressors [30,45–47].

643 Libraries for the six strains that did not carry suppressors in *DHR1*, *IMP4*, *UTP2* or *UTP14*
644 were prepared and sequenced on an Illumina NextSeq 500 platform by the Genomic Sequencing
645 and Analysis Facility at the University of Texas at Austin. The quality of the resultant reads was
646 assessed using FastQC (v0.10.1) [http://www.bioinformatics.babraham.ac.uk/projects/fastqc/],
647 and subsequently processed using TrimGalore (v1.14)
648 [http://www.bioinformatics.babraham.ac.uk/projects/trim_galore/] to discard low-quality
649 sequences and adapters. The processed reads were aligned using Bowtie2 (v2.3.4) [81] using the
650 default settings for paired-end reads. The resultant files were further processed with SAMtools
651 (v0.1.18) [82] and BCFtools (v0.1.17) [83] to generate variant call format files. VCFtools (v0.1.16)
652 [84] was used to filter out variants with low quality scores (Quality value < 100) and to compare
653 samples pairwise to identify mutations unique to each suppressed strain. This analysis revealed
654 single point mutations within *BMS1* and *RPS28A* that were confirmed by Sanger sequencing. The
655 *bms1* and *rps28a* variants were subsequently cloned into centromeric vectors and, as with all
656 other *bud23*Δ suppressors that we have identified, the *rps28A* and *bms1* mutants were dominant
657 (data not shown). All mutant strains isolated in this screen are listed in Table 1.
658

659 **Identification of mutations in *UTP2* that suppress *bud23*Δ.** Random mutations in *UTP2*
660 were generated by error-prone PCR using *Taq* polymerase and pAJ2595 as the template and
661 oligos that hybridize to the upstream and downstream sequences of *UTP2*. The restriction
662 enzymes *Eco*RI and *Sph*I were used to linearize the vector pAJ2595 and the linearized vector was,
663 co-transformed with the mutant amplicon into AJY2161, and plated onto SD-Uracil media to
664 allow recombination of the mutant amplicon into the pAJ2595 backbone. Colonies displaying a
665 suppressed phenotype were isolated; vectors were rescued from yeast and sequenced after
666 confirming that the vectors conferred suppression.
667
668 **Affinity purification.** Cells were cultured as described in the Northern blotting and mass
669 spectrometry subsections below. All steps were carried out on ice or at 4°C. Cells were washed
670 with Lysis Buffer (50 mM Tris-HCl pH 7.6 (25°C), 100 mM KCl, 5 mM $MgCl_2$, 5 mM beta-
671 mercaptoethanol (βME), 1 mM each of PMSF and Benzamidine, and 1 µM each of leupeptin and
672 pepstatin) supplemented with EDTA-free Pierce Protease Inhibitor Mini Tablet cocktail (Thermo
673 Scientific), then resuspended in 1 volume Lysis Buffer. Extracts were generated by glass bead lysis
674 and clarified at 18,000*g* for 15 minutes. Clarified extracts were normalized according to A_{260} and
675 supplemented with 0.1% TritonX-100. Normalized extracts were incubated for 1.5 hours with
676 rabbit IgG (Sigma) coupled to Dynabeads (Invitrogen), prepared as previously described [85].
677 Following binding, the beads were washed thrice with Wash Buffer (Lysis Buffer supplemented
678 with 0.1% TritonX-100). The beads were resuspended in Elution Buffer (Wash Buffer
679 supplemented with TEV protease and Murine RNase Inhibitor (New England Biolabs)) and the

680 bound Enp1-TAP containing complexes were eluted for 1.5 – 2 hours. The resultant eluates were
681 handled as described in the Northern blotting and mass spectrometry subsections below.
682
683 **Northern blot analysis.** For analysis of rRNA processing in whole cell extract (WCE), strains
684 were cultured overnight in YPD media to saturation. Cell cultures were diluted into YPD at a
685 starting OD_{600} of 0.1 and cultured to mid-exponential phase (OD_{600} ~0.4-0.5) before collection
686 and storage at -80°C prior to lysis. For analysis of affinity purified RNAs, strains AJY2665 and
687 AJY4395 were cultured overnight in YPD media to saturation. Cells were diluted into YPD at a
688 starting OD_{600} of 0.05 and cultured for three hours. Cultures were treated with 0.5 mM auxin for
689 2 hours at 30°C, centrifuged, and frozen in liquid nitrogen. Affinity purification was performed as
690 described above. Affinity purified and WCE RNAs were isolated using the acid-phenol-chloroform
691 method as previously described (Zhu et al. 2016). RNAs were electrophoresed through 1.2%-
692 agarose MOPS 6% formaldehyde gel. Northern blotting was performed as previously described
693 (Li et al. 2009) using the oligo probes listed in the legends of Figures 2 and 7, and signal was
694 detected by phosphoimaging on a GE Typhoon FLA9500.
695
696 **Mass spectrometry and analysis.** Strains AJY2665 and AJY4395 were cultured as
697 described in the Northern blot analysis subsection. Affinity purifications were performed as
698 described above. To isolate factors associated with only pre-ribosomal particles, the eluate was
699 overlaid onto a sucrose cushion (15% D-sucrose, 50 mM Tris-HCl pH 7.6 (25°C), 100 mM KCl, 5
700 $MgCl_2$) then centrifuged at 70,000 rpm for 15 min in a Beckman Coulter TLA100 rotor. Following,
701 the pellets were precipitated with 15% trichloroacetic acid (TCA), washed with acetone and dried,

702 and resuspended in 1X Laemmli buffer. Approximately equivalent amounts of protein were either
703 fully separated on SDS-PAGE gels for excision of individual species or electrophoresed slightly
704 into a NuPAGE Novex 4%–12% Bis-Tris gel for analysis of the entire affinity purification. Peptides
705 were recovered from in-gel Trypsin digestion and prepared for identification by mass
706 spectrometry as previously described [33]. The resultant peptides were identified at The
707 University of Texas at Austin Proteomics Facility by LC-MS/MS on a Thermo Orbitrap Fusion 1
708 with either a 30 minute or 1 hour run time for identification of single species or complex sample,
709 respectively. Mass spectrometry data were processed in Scaffold v4.8.3 (Proteome Software,
710 Inc.). A protein threshold of 99% minimum with two peptides minimum and peptide threshold of
711 1% false discovery rate was applied. The data were exported, and custom Python 2.7 scripts were
712 used to calculate the relative spectral abundance factor (RSAF) for each protein by dividing the
713 total number of spectral counts by the molecular weight. Values for each protein were
714 normalized to the bait, Enp1, to reflect relative stoichiometry. Supplemental File 2 contains
715 relevant spectral counts and processed data from the mass spectrometry experiments.
716
717 **Sucrose density gradient analysis.** For polysome profile analysis of the suppressors of
718 *bud23*Δ, BY4741, AJY2676, AJY3744, AJY4529, AJY4531, and AJY4535 were cultured overnight in
719 YPD to saturation. Cultures were diluted into YPD at a starting OD_{600} of 0.02 and cultured to early
720 exponential phase (OD_{600}~0.10-0.13) and then treated with cycloheximide (CHX) at 100 µg/ml for
721 10 minutes at 30°C to inhibit translation. After centrifugation cells were frozen in liquid nitrogen
722 and stored at -80°C. Cells were washed and resuspended in Lysis Buffer (50 mM Tris-HCl pH 7.6
723 (25°C), 100 mM KCl, 5 mM $MgCl_2$, 7 mM βME, 100 µg/mL CHX, 1 mM each of PMSF and

724 Benzamidine, and 1 µM each of leupeptin and pepstatin). Extracts were prepared by glass bead
725 lysis and clarified by centrifugation for 15 minutes at 18,000*g* at 4°C. 4.5 A_{260} units of clarified
726 extract were loaded onto 7-47% sucrose gradients made in the same buffer lacking protease
727 inhibitors. Gradients were subjected to ultracentrifugation for 2.5 hours at 40,000 rpm in a
728 Beckman SW40 rotor. The gradients were subjected to continuous monitoring at 254 nm using
729 an ISCO Model 640 fractionator.

730 For analysis of the sedimentation of factors in the absence of Bud23, AJY2665 and
731 AJY4395 were cultured overnight to saturation. Cells were diluted into YPD at a starting OD_{600} of
732 0.05 and cultured for three hours (OD_{600} =~0.08-0.1). Cultures were treated with 0.5 mM auxin
733 for 2 hours at 30°C, then treated with CHX at 100 µg/mL for 10 minutes at 30°C. Cells were
734 harvested and stored as described above. Cells were washed and resuspended in Lysis Buffer
735 supplemented with an EDTA-free Pierce Protease Inhibitor Mini Tablet cocktail (Thermo
736 Scientific). Extracts were generated, and nine A_{260} units were loaded onto sucrose gradients and
737 subject to ultracentrifugation as described above. Gradients were fractionated into 600 µL
738 fractions with continuous monitoring at 254 nm using an ISCO Model 640 fractionator. Each
739 fraction was split in half to collect proteins and RNAs. Proteins were precipitated using 15% TCA
740 as described previously [33]. One-fifth of protein from each half fraction was separated on SDS-
741 PAGE gels and subjected to Western blotting. RNAs were precipitated as described previously
742 [86] supplemented with 10 µg of glycogen. One-third of RNA from each half fraction was
743 subjected to Northern blotting as described above.
744

745 **Western blot analysis.** Primary antibodies used in this study were anti-c-Myc monoclonal
746 9e10 (Biolegend), anti-HA (Biolegend), anti-Bud23 (C. Wang), anti-Rps24 (our laboratory), anti-
747 Glucose-6-phosphate dehydrogenase (Sigma ImmunoChemicals), and anti-Imp4 (S. Baserga).
748 Secondary anti-bodies were goat anti-mouse antibody-IRDye 800CW (Li-Cor Biosciences), goat
749 anti-rabbit antibody-IRDye 680RD (Li-Cor Biosciences), and goat anti-rabbit antibody-HRP
750 (Jackson Immunoresearch Laboratories). The blots in Figs. 3D, 3F, 5C, and 6B were imaged with
751 an Odyssey CLx infrared imaging system (Li-Cor Biosciences) using Image Studio (Li-Cor
752 Biosciences). The blots in Fig. 6C were imaged using SuperSignal West Pico PLUS
753 Chemiluminescent Substrate (Thermo Scientific) and exposed to film.
754
755 **Molecular visualization.** All images of SSU Processome and Dhr1 structures are from PDB
756 ascension codes 5WLC and 6H57, respectively. The structures of GDPNP- and GDP-bound EF-Tu
757 are from PDB ascension codes 1B23 and 1EFC, respectively. Molecular visualizations were
758 generated using MacPyMOL: PyMOL v1.8.2.1 Enhanced for Mac OS X (Schrödinger LLC).
759

760 ## Figure legends

761 **Figure 1. Extragenic suppressors of *bud23*Δ reveal an interaction network that connects the 3'**
762 **basal subdomain to the U3-18S heteroduplexes.** (A) A secondary structure map of the 18S rRNA
763 that indicates the position of the 3' basal subdomain (dark gray) and the central pseudoknot (CPK;
764 deep olive). (B) The position of the 3' basal subdomain (dark gray) within the context of the SSU
765 Processome structure (light gray). (C) Factors harboring mutations that suppress *bud23*Δ and are
766 resolved in the SSU Processome (PDB 5WLC) cluster around the 3' basal subdomain and the U3-

767 Box A'-18S heteroduplex that Dhr1 unwinds. Shown are: Bms1 (forest green), Imp4 (blue), Rps28
768 (cyan), Utp2 (orange), Utp14 (brown), U3 (deep purple), 18S rRNA (deep olive), 3' basal
769 subdomain (dark gray). (D) Zoomed view of factors in C showing contacts amongst each other,
770 the 3' basal subdomain, and the U3-Box A'-18S heteroduplex. N- and C-terminal domains, NTD
771 and CTD, respectively. The U3-18S heteroduplexes are shown as U3 Box A and U3 Box A'.
772 Guanosine 1575 (G1575, red) is shown as a marker for the binding site of Bud23. (E) Tabulation
773 of the number of unique mutations found in each extragenic suppressor of *bud23*Δ. Newly
774 identified mutations (novel) and previously identified (known) [30,45–47]. The complete list of
775 these mutations is available in Supplemental File 1. (F) Summary of the genetic and physical
776 interactions amongst the suppressors of *bud23*Δ. Factors are indicated as nodes; genetic and
777 physical interactions are shown as dashed and solid edges, respectively.
778
779 **Figure 2. The Imp4 and Rps28A mutations primarily map to their interfaces with the 3' basal**
780 **subdomain.** (A) Point mutations within *imp4* and *rps28a* suppressed the growth defect of *bud23*Δ
781 as shown by 10-fold serial dilutions of wild-type cells (BY4741), *bud23*Δ (AJY2676), and *bud23*Δ-
782 suppressed cells spotted on YPD media and grown for two days at 30°C. (B) Rps28 and the Brix
783 domain of Imp4 interact with the 3' basal subdomain RNA, while the NTD of Imp4 makes contacts
784 with its Brix domain and the U3-18S heteroduplexes. G1575, the binding site of Bud23, is shown
785 for reference. The regions where the mutated residues map are indicated by magenta and green
786 dashed boxes for the rRNA interaction and the NTD interaction, respectively. Factors are colored
787 the same as in Fig. 1. (C) Residues mutated in Rps28 and Imp4 Brix domain map to interaction
788 interfaces with the 3' basal subdomain RNA (magenta sticks). (D) Several residues mutated in

789 Imp4 map to an intramolecular interaction between the Brix and NTD of Imp4 (green sticks). (E)
790 Suppressing mutations in *imp4* and *rps28a* partially restored A2 processing and 18S rRNA levels
791 in *bud23*Δ cells. RNA processing intermediates were detected by Northern blotting on RNAs
792 extracted from wild-type (WT), *bud23*Δ, and *bud23*Δ-suppressed cells cultured to exponential
793 phase at 30°C in liquid YPD. P32-radiolabeled probes (Table 3) hybridized to the indicated regions.
794 The 25S and 18S rRNAs were detected by methylene blue staining of the RNAs prior to
795 oligonucleotide hybridization. (F) The *imp4* and *rps28a* mutations partially restored 40S
796 biogenesis as shown by polysome profiles after separation of extracts on sucrose density
797 gradients from wild-type, *bud23*Δ, and *bud23*Δ-suppressed cells cultured to exponential phase at
798 30°C in liquid YPD media.
799
800 **Figure 3. The mutations in Utp2 disrupted its interaction with Imp4.** (A) Spontaneous point
801 mutations within *utp2* partially suppressed the growth defect of *bud23*Δ as shown by 10-fold
802 serial dilutions of wild-type cells (BY4741), *bud23*Δ (AJY2676), and *bud23*Δ-suppressed cells
803 spotted on YPD media and grown for two days at 30°C. (B) Additional point mutations in *UTP2,*
804 generated by error-prone PCR, also suppressed the growth defect of *bud23*Δ (left) and
805 complemented loss of *UTP2* (right) as shown by 10-fold serial dilutions of *bud23*Δ (AJY2676) and
806 *PGAL10-UTP2* (AJY4175) cells containing either empty vector, or vectors encoding the indicated
807 alleles of *UTP2* spotted on SD-Leu media containing glucose and grown for two days at 30°C. (C)
808 Several of the mutations in Utp2 map to residues (green sticks) located within its NTD (orange)
809 that interacts with the Brix domain of Imp4 (blue) adjacent to the 3' basal subdomain RNA (gray).
810 (D) Left: Yeast two-hybrid interaction assay between Imp4 and wild-type (WT) or mutant Utp2.

811 Strains carrying the indicated constructs were patched onto Leu- Trp- (L-W-) and Leu-Trip-His- (L-
812 W-H-) media supplemented with 2 mM 3-Amino-1,2,4-triazole (3AT) (AD, Gal4 activation domain;
813 BD, Gal4 DNA binding domain). Right: Western blot analysis of the wild-type and mutant Utp2-
814 AD-HA proteins using equivalent amounts of total protein extracts. Glucose-6-phosphate
815 dehydrogenase (G6PDH) was used as a loading control. (E) Top: F58 of Utp2 (green sticks) fits
816 into a hydrophobic pocket in the Brix domain of Imp4 (surface representation). Bottom: The
817 *bud23*Δ-suppressing mutations V170F and P252L of Imp4 (magenta sticks) line this pocket. Imp4
818 and Utp2 are colored blue and orange, respectively. (F) Top: Yeast two-hybrid interaction assay
819 between Utp2 and wild-type or mutant Imp4. Strains carrying the indicated constructs were
820 patched onto L-W- and L-W-H- media supplemented with 6 mM 3AT. Bottom: Western blot
821 analysis of the wild-type and mutant BD-myc-Imp4 proteins in equivalent amounts of total
822 protein extract is shown. G6PDH was used as a loading control.
823
824 **Figure 4. The mutations in the GTPase Bms1 that suppress *bud23*Δ are poised to modulate its**
825 **conformational state.** (A) Spontaneous point mutations within *BMS1* suppressed the growth
826 defect of *bud23*Δ as shown by 10-fold serial dilutions of wild-type cells (BY4741), *bud23*Δ
827 (AJY2676), and *bud23*Δ cells carrying the indicated *bms1* mutations spotted on YPD media and
828 grown for two days at 30°C. (B) The *bms1* mutations partially restored A2 processing and 18S
829 rRNA production in *bud23*Δ cells as shown by Northern blotting of RNAs extracted from wild-
830 type, *bud23*Δ, and *bud23*Δ-suppressed cells as described in Fig. 2E. (C) The *bms1* mutations
831 partially restored 40S biogenesis as shown by the analysis of the polysome profiles from the
832 indicated strains as described in Fig. 2F. (D) Top: Primary structure of Bms1 with domains (in

833 different shades of green), interacting regions and *bud23*Δ suppressing mutations annotated;
834 regions not resolved in SSU Processome structures are indicated in light gray. Bottom: The partial
835 structure of Bms1 (from PDB 5WLC) in the context of the SSU Processome is shown. Domains IV
836 and V extend from its GTPase core (domains I – III) to contact the RNAs of the 3' basal subdomain
837 (gray) and the U3-18S heteroduplexes (pink/gold), respectively. (E) At the 3' basal subdomain,
838 Domain IV of Bms1 also contacts the CTDs of Utp2 (orange) and Imp4 (blue). (F) The mutated
839 residues D124, D843, A903, and S1020 in Bms1 map to inter-domain contacts with the
840 unstructured strand of domain V that connects it to domain IV.
841
842 **Figure 5. Most of the Dhr1 mutations map to surface residues of its RecA domains.** (A) A cartoon
843 of the primary structure of Dhr1 is shown. The domains of Dhr1 are annotated by color: NTD, N-
844 terminal domain (light gray); RecA1/2, Recombination protein A1/2 (blue/green); WH, winged-
845 helix (yellow); HB, helical bundle (orange); OB, oligonucleotide-binding fold (brown); CTD, C-
846 terminal domain (light red). Unstructured regions are colored as light gray. Mutations reported
847 here (novel) and previously (known) [46] are indicated as black and magenta, respectively.
848 Numbering indicates residue numbering of yeast Dhr1. (B) The structure of yeast Dhr1 (PDB
849 6H57) with relevant features colored as described in panel A. Catalytic residues involved in ATP
850 hydrolysis are denoted as red sticks for reference. (C) The majority of the mutated residues map
851 to the surfaces of the RecA domains. Mutated residues are shown as black and magenta sticks as
852 described for panel A. The positions of the residues that were used to test loss-of-interaction
853 with Utp14 in panel D are indicated. (D) Top: Yeast two-hybrid interaction data between AD-HA-
854 Utp14 and wild-type (WT) or mutant BD-myc-Dhr1 are shown. Strains carrying the indicated

855 constructs were patched onto Leu- Trp- (L-W-) and Leu-Trip-His- (L-W-H-) media supplemented
856 with 10 mM 3-Amino-1,2,4-triazole (3AT) (AD-HA, GAL4AD-HA; BD-myc, GAL4BD-myc). Bottom:
857 Western blot analysis of the wild-type and mutant BD-myc-Dhr1 proteins using equivalent
858 amounts of total protein extracts is shown. Glucose-6-phosphate dehydrogenase (G6PDH) was
859 used as a loading control.
860
861 **Figure 6. Imp4 and Enp1 accumulate with pre-40S upon Bud23 depletion.** (A) The genomic
862 fusion of an auxin-inducible degron (AID) to the C-terminus of Bud23 rendered cells sensitive to
863 auxin, with a growth defect comparable to *bud23*Δ. 10-fold serial dilutions of wild-type
864 (AJY2665), *BUD23-AID* (AJY4395), and *bud23*Δ (AJY3156) cells were spotted on YPD media with
865 and without 0.5 mM auxin and grown for two days at 30°C. (B) Western blot of time-course of
866 depletion of Bud23-AID, using equivalent amounts of total protein extract from AJY2665 or
867 AJY4395 cells cultured to exponential phase then harvested prior to or after the addition of 0.5
868 mM auxin for the indicated time (WT; wild-type). G6PDH was used as a loading control. (C) The
869 sucrose density gradient sedimentation of Enp1-TAP, Imp4, and Rps24 in the presence (upper
870 panel) or absence (lower panel) of Bud23. Extracts were prepared from + Bud23 (AJY2665) and -
871 Bud23 (AJY4395) cells treated with 0.5 mM auxin for two hours and separated on sucrose density
872 gradients prior to fractionation. Proteins from each fraction were precipitated and subjected to
873 Western blot analysis.
874
875 **Figure 7. Composition of 40S precursors purified in the absence of Bud23.** (A) Coomassie-
876 stained gel of proteins that co-purified with Enp1-TAP in the presence (+) or absence (-) of Bud23.

877 Pre-ribosomal particles were enriched by overlaying eluate onto sucrose cushions followed by
878 ultracentrifugation. Individual species that showed clear enrichment or depletion were excised
879 and identified by mass spectrometry and are indicated in blue or black text, respectively. The
880 asterisks (*) denote proteins that also appeared in the analysis described in Fig. S6. (B) The rRNA
881 processing intermediates and U3 snoRNA that co-purified with Enp1-TAP in the presence (+) or
882 absence (-) of Bud23 were detected by Northern blotting using the indicated probes.
883 Oligonucleotides are listed in Table 3.
884
885 **Figure 8. Models for Bud23 function in SSU Processome progression.** (A) The Bud23-Trm112
886 subcomplex (light yellow and light blue, respectively) enters a partially disassembled SSU
887 Processome to establish a state competent for productive unwinding of U3 snoRNA (gray) by
888 Dhr1, to allow folding of the central pseudoknot and compaction of the 5' (blue), central (yellow),
889 3' major (magenta), and 3' minor (green) domains onto one another to yield an early pre-40S.
890 Only the rRNA, U3 snoRNA, and Bud23-Trm112 subcomplex are shown for simplicity. The U3-18S
891 rRNA heteroduplexes that Dhr1 unwinds are indicated by a dashed box. The rRNAs of the SSU
892 Processome (left) are a composite of two structures (PDB: 5WLC, 5WYK), and the Bud23-Trm112
893 subcomplex and the rRNA of the pre-40S (right) are from an early human pre-40S (PDB: 6G4W).
894 The middle image is an overlay of the left and right images with the partially disassembled SSU
895 Processome grayed out. (B) A cartoon 2-dimensional projection of Fig. 1D showing factors that
896 surround the 3' basal subdomain (gray) and U3-18S heteroduplexes (magenta/gold). During
897 assembly of the SSU Processome, multiple contacts are formed amongst Bms1 (green), Imp4
898 (blue), and Utp2 (orange). These three proteins contain long helical extensions that support the

899 U3-18S heteroduplexes but block their access by Dhr1 (light blue). Bms1, Imp4, and Utp2 all have
900 extensive interactions with the 3' basal subdomain rRNA that connect events here to the U3-18S
901 heteroduplexes. After partial SSU Processome disassembly, Bud23 (yellow) binds to the 3' basal
902 subdomain and signals to Bms1 to activate its GTPase domain. This, in turn, leads to
903 conformational changes that displace the helical extensions of these proteins away from the U3-
904 18S heteroduplexes allowing Dhr1 to gain access so that it can unwind it.
905

906 ## Supplemental figure legends

907 **Figure S1. Schematic of rRNA processing relevant to 40S production in *S. cerevisiae.***
908 Endonucleolytic processing of the pre-18S rRNA at sites A0, A1, and A2 (or A3) occurs within the
909 context of the SSU Processome. Events occurring co- or post-transcriptionally are denoted by
910 blue and red scissors, respectively. Cleavage at either the A2 or A3 sites liberates the SSU
911 precursors from the LSU precursors containing the 27SA2 and 27SA3 rRNA intermediates,
912 respectively. In rapidly dividing cells processing of A0, A1, and A2 appear to occur co-
913 transcriptionally in a sequential order to produce the 20S rRNA intermediate. The RNA Exosome
914 exonucleolytically degrades the A0- and A1-cleaved 5' ETS fragments. When A1 or A2 cleavage is
915 delayed, post-transcriptional cleavage at A3 occurs to produce the 22S or 21S rRNA, and A1 and
916 A2 cleavage instead occur post-transcriptionally to generate the 20S rRNA. When SSU
917 Processome function is entirely precluded, cleavage at A3 produces the 23S rRNA that becomes
918 degraded. The 20S rRNA is a component of pre-40S intermediates that are exported to the
919 cytoplasm where an endonuclease processes the D site to yield the 18S rRNA.
920

921 **Figure S2. Secondary structure diagram of the 18S rRNA.** The 18S rRNA is divided into four main
922 domains: the 5' domain (blue), central domain (gold), 3' major domain (purple and black), and
923 the 3' minor domain (green). The 3' basal subdomain (black) is a sub-region of the 3' major
924 domain that forms during the assembly of the SSU Processome [17], and contains the binding
925 site for Bud23. The base methylated by Bud23, guanosine 1575 (G1575, red) is indicated. The
926 position of the Central Pseudoknot (CPK, gray) is also pictured.
927
928 **Figure S3. The position of Utp14 and the binding site of Dhr1 within the SSU Processome.** (A)
929 The location of the resolved segments of Utp14 (brown) in the SSU Processome. A contour line
930 indicates the unresolved region of Utp14 where the Dhr1-interaction surface and *bud23*Δ-
931 suppressing mutations are located. The U3 snoRNA binding site of Dhr1 and U3 mutations that
932 suppress a cold-sensitive Dhr1 mutant [29] are indicated by cyan and black sticks, respectively.
933 Bms1, Imp4, Rps28, Utp2, and the 3' basal subdomain RNA are shown for reference. (B) A cartoon
934 of Utp14 primary structure indicating the position of its resolved portions and the *bud23*Δ-
935 suppressing mutations reported here (black) and previously (light blue) within its Dhr1-
936 activaction loop [30].
937
938 **Figure S4. Comparison of the structure of Bms1 to the conformational states of EF-Tu.** (A)
939 Structural alignment of EF-Tu bound to the non-hydrolysable GTP analog, GDPNP (slate blue, PDB
940 1B23) to domain I of Bms1 (from PDB 5WLC) is shown. Bms1 is colored by domains as in Fig. 4D;
941 the GTP analog and magnesium ion bound to EF-Tu are shown as orange sticks and green sphere.
942 Structures are shown individually (left, middle) and as an overlay (right). (B) A view of domains II

943 and III of Bms1 compared to those of EF-Tu shows that the two domains adopt beta barrels in
944 similar conformations. (C) GDPNP-bound EF-Tu forms a complex with tRNA, while GDP-bound EF-
945 Tu (deep purple, PDB 1EFC) does not. (D) Conformational differences in the beta-barrel domains
946 of GDP and GTP-bound EF-Tu suggest that these domains rotate away from one another upon
947 GTP hydrolysis to promote tRNA release. (E) The amino-acyl tRNA contacts GDPNP-bound EF-Tu
948 through its two beta barrel domains. (F) Bms1 in the same orientation as EF-Tu in panel E. The
949 unstructured loop of domain V that connects it to domain IV (denoted by the black arrow) and
950 an N-terminal helix of Mpp10 (red) contacts domains II and III of Bms1 in a manner reminiscent
951 of how tRNA interacts with GDPNP-bound EF-Tu. The mutated residues that suppress *bud23*Δ are
952 shown as magenta sticks.
953
954 **Figure S5. Proteomic compositions of 40S pre-cursors from cells with or without Bud23.** Related
955 to Figure 7. A heatmap of SSU biogenesis proteins that co-immunoprecipitated with Enp1-TAP in
956 the presence (+) or absence (-) of Bud23 is shown. The scale spanning from 0 (white) to 1 (cyan)
957 reflects the relative spectral abundance factor (RSAF). The RSAF was calculated by first
958 normalizing the total number of spectral counts identified for a given protein to its molecular
959 weight; these values were further normalized to the bait, Enp1, to reflect stoichiometry. RSAF
960 values for each protein are shown within each cell. For each protein, the number of spectral
961 counts identified in the presence or absence of Bud23 are shown in parentheses, respectively.
962 Proteins that showed a significant increase or decrease relative to the + Bud23 sample and are
963 listed in Fig. S6 are denoted by an asterisks (*) colored blue or black, respectively. Proteins are
964 grouped according to [7] or by known function. Heatmaps were generated in Graphpad Prism

965 version 8.3.0 (328) for Mac iOS. The complete data for this figure are available in Supplemental
966 File 2.
967
968 **Figure S6. 40S biogenesis factors whose association with 40S pre-cursors significantly changed**
969 **upon Bud23-depletion.** Related to Figures 7 and S5. Mass spectrometry analysis of total proteins
970 that co-precipitated with Enp1. Proteins that showed a significant log2 fold-change difference in
971 the absence or presence or Bud23 are shown. Total number of peptides identified for each
972 protein was normalized to molecular weight then further normalized to the bait to generate RSAF
973 values (see Methods) which were used to calculate the log2 fold-change between the mutant
974 and wild-type samples. Proteins displaying a ± 0.5-fold change or more with a difference of
975 greater than 10 total spectral counts are plotted. Proteins are grouped according to when they
976 first bind to pre-ribosomes [7]. The complete mass spectrometry data are available in
977 Supplemental File 2.
978

979 ## Tables

980 **Table 1: Yeast strains used in this study.**

Strain	Genotype	Reference
AJY2665	*MATa his3Δ1 leu2Δ0 met15Δ0ura3Δ0 ENP1-TAP::HIS3MX6*	[87]
AJY2161	*MATa his3Δ1 leu2Δ0 ura3Δ0 lys2Δ0 met15Δ0 bud23Δ::KanMX*	[39]
AJY2676	*MATa his3Δ1 leu2Δ0 ura3Δ0 lys2Δ0 met15Δ0 bud23Δ::CloNAT*	This study & [47].
AJY3156	*MATa his3Δ1 leu2Δ0 met15Δ0ura3Δ0 ENP1-TAP::HIS3MX6 bud23Δ::KanMX*	This study.
AJY3581	*MATa his3Δ1 leu2Δ0 ura3Δ0 lys2Δ0 met15Δ0 bud23Δ::KanMX utp2-A2D*	[45]
AJY3512	*MATa his3Δ1 leu2Δ0 ura3Δ0 lys2Δ0 met15Δ0 bud23Δ::KanMX*	This study & [47].

	imp4-V170F	
AJY3579	*MATa his3Δ1 leu2Δ0 ura3Δ0 lys2Δ0 met15Δ0 bud23Δ::KanMX imp4-R94L*	This study & [47].
AJY3580	*MATa his3Δ1 leu2Δ0 ura3Δ0 lys2Δ0 met15Δ0 bud23Δ::KanMX imp4-N118K*	This study & [47].
AJY3741	*MATa his3Δ1 leu2Δ0 ura3Δ0 lys2Δ0 met15Δ0 bud23Δ::KanMX imp4-T92I*	This study & [47].
AJY3742	*MATa his3Δ1 leu2Δ0 ura3Δ0 lys2Δ0 met15Δ0 bud23Δ::KanMX imp4-R116M*	This study & [47].
AJY3743	*MATa his3Δ1 leu2Δ0 ura3Δ0 lys2Δ0 met15Δ0 bud23Δ::KanMX imp4-S93T*	This study & [47].
AJY3744	*MATa his3Δ1 leu2Δ0 ura3Δ0 lys2Δ0 met15Δ0 bud23Δ::KanMX imp4-R94S*	This study & [47].
AJY3745	*MATa his3Δ1 leu2Δ0 ura3Δ0 lys2Δ0 met15Δ0 bud23Δ::KanMX imp4-N118D*	This study & [47].
AJY4501	*MATa his3Δ1 leu2Δ0 ura3Δ0 lys2Δ0 met15Δ0 bud23Δ::CloNAT imp4-H159R*	This study.
AJY4502	*MATa his3Δ1 leu2Δ0 ura3Δ0 lys2Δ0 met15Δ0 bud23Δ::CloNAT utp2-L9S*	This study.
AJY4503	*MATa his3Δ1 leu2Δ0 ura3Δ0 lys2Δ0 met15Δ0 bud23Δ::CloNAT utp14-W794L*	This study.
AJY4504	*MATa his3Δ1 leu2Δ0 ura3Δ0 lys2Δ0 met15Δ0 bud23Δ::CloNAT imp4-R99L*	This study.
AJY4505	*MATa his3Δ1 leu2Δ0 ura3Δ0 lys2Δ0 met15Δ0 bud23Δ::CloNAT imp4-N121I*	This study.
AJY4506	*MATa his3Δ1 leu2Δ0 ura3Δ0 lys2Δ0 met15Δ0 bud23Δ::CloNAT imp4-Y77C*	This study.
AJY4507	*MATa his3Δ1 leu2Δ0 ura3Δ0 lys2Δ0 met15Δ0 bud23Δ::CloNAT imp4-S101W*	This study.
AJY4508	*MATa his3Δ1 leu2Δ0 ura3Δ0 lys2Δ0 met15Δ0 bud23Δ::CloNAT imp4-H208D*	This study.
AJY4509	*MATa his3Δ1 leu2Δ0 ura3Δ0 lys2Δ0 met15Δ0 bud23Δ::CloNAT imp4-R94C*	This study.
AJY4510	*MATa his3Δ1 leu2Δ0 ura3Δ0 lys2Δ0 met15Δ0 bud23Δ::CloNAT imp4-H156D*	This study.
AJY4511	*MATa his3Δ1 leu2Δ0 ura3Δ0 lys2Δ0 met15Δ0 bud23Δ::CloNAT*	This study.

	imp4-R99H	
AJY4512	*MATa his3Δ1 leu2Δ0 ura3Δ0 lys2Δ0 met15Δ0 bud23Δ::CloNAT imp4-R146G*	This study.
AJY4513	*MATa his3Δ1 leu2Δ0 ura3Δ0 lys2Δ0 met15Δ0 bud23Δ::CloNAT W791L*	This study.
AJY4514	*MATa his3Δ1 leu2Δ0 ura3Δ0 lys2Δ0 met15Δ0 bud23Δ::CloNAT dhr1-D408Y*	This study.
AJY4515	*MATa his3Δ1 leu2Δ0 ura3Δ0 lys2Δ0 met15Δ0 bud23Δ::CloNAT dhr1-G432R*	This study.
AJY4516	*MATa his3Δ1 leu2Δ0 ura3Δ0 lys2Δ0 met15Δ0 bud23Δ::CloNAT dhr1-S511Y*	This study.
AJY4517	*MATa his3Δ1 leu2Δ0 ura3Δ0 lys2Δ0 met15Δ0 bud23Δ::CloNAT dhr1-G434D*	This study.
AJY4518	*MATa his3Δ1 leu2Δ0 ura3Δ0 lys2Δ0 met15Δ0 bud23Δ::CloNAT dhr1-E397D*	This study.
AJY4519	*MATa his3Δ1 leu2Δ0 ura3Δ0 lys2Δ0 met15Δ0 bud23Δ::CloNAT dhr1-R596G*	This study.
AJY4520	*MATa his3Δ1 leu2Δ0 ura3Δ0 lys2Δ0 met15Δ0 bud23Δ::CloNAT dhr1-D566Y*	This study.
AJY4521	*MATa his3Δ1 leu2Δ0 ura3Δ0 lys2Δ0 met15Δ0 bud23Δ::CloNAT dhr1-A804D*	This study.
AJY4522	*MATa his3Δ1 leu2Δ0 ura3Δ0 lys2Δ0 met15Δ0 bud23Δ::CloNAT dhr1-R596S*	This study.
AJY4523	*MATa his3Δ1 leu2Δ0 ura3Δ0 lys2Δ0 met15Δ0 bud23Δ::CloNAT dhr1-M857I*	This study.
AJY4524	*MATa his3Δ1 leu2Δ0 ura3Δ0 lys2Δ0 met15Δ0 bud23Δ::CloNAT dhr1-R563M*	This study.
AJY4525	*MATa his3Δ1 leu2Δ0 ura3Δ0 lys2Δ0 met15Δ0 bud23Δ::CloNAT dhr1-R13G*	This study.
AJY4526	*MATa his3Δ1 leu2Δ0 ura3Δ0 lys2Δ0 met15Δ0 bud23Δ::CloNAT dhr1-E1037Q*	This study.
AJY4527	*MATa his3Δ1 leu2Δ0 ura3Δ0 lys2Δ0 met15Δ0 bud23Δ::CloNAT dhr1-E1037K*	This study.
AJY4529	*MATa his3Δ1 leu2Δ0 ura3Δ0 lys2Δ0 met15Δ0 bud23Δ::CloNAT bms1-D843V*	This study.
AJY4530	*MATa his3Δ1 leu2Δ0 ura3Δ0 lys2Δ0 met15Δ0 bud23Δ::CloNAT*	This study.

	dhr1-F594L	
AJY4531	*MATa his3Δ1 leu2Δ0 ura3Δ0 lys2Δ0 met15Δ0 bud23Δ::CloNAT rps28a-G24D*	This study.
AJY4532	*MATa his3Δ1 leu2Δ0 ura3Δ0 lys2Δ0 met15Δ0 bud23Δ::CloNAT bms1-D124Y*	This study.
AJY4533	*MATa his3Δ1 leu2Δ0 ura3Δ0 lys2Δ0 met15Δ0 bud23Δ::CloNAT bms1-A903P*	This study.
AJY4535	*MATa his3Δ1 leu2Δ0 ura3Δ0 lys2Δ0 met15Δ0 bud23Δ::CloNAT bms1-G813S*	This study.
AJY4536	*MATa his3Δ1 leu2Δ0 ura3Δ0 lys2Δ0 met15Δ0 bud23Δ::CloNAT imp4-P252L*	This study.
AJY4537	*MATa his3Δ1 leu2Δ0 ura3Δ0 lys2Δ0 met15Δ0 bud23Δ::CloNAT bms1-S1020L*	This study.
AJY4395	*MATa his3Δ1 leu2Δ0 met15Δ0ura3Δ0 ENP1-TAP::HIS3MX6 BUD23-AID-HA::OsTIR1::LEU2*	This study.
BY4741	*MATa his3Δ1 leu2Δ0 met15Δ0 ura3Δ0*	Open Biosystems
PJ69-4a	*MATa trp1-901 leu2-3,112 ura3-52 his3-200 gal4Δ gal80Δ LYS2::GAL1-HIS3 GAL2-ADE2 met2::GAL7*-lacZ	[88]
PJ69-4alpha	MATalpha trp1-901 leu2-3,112 ura3-52 his3-200 gal4Δ gal80Δ LYS2::GAL1-HIS3 GAL2-ADE2 met2::GAL7-lacZ	[88]

Table 2: Plasmids used in this study.

Plasmid	Description	Reference
pAJ2321	*GAL4AD-HA-UTP14 LEU2 2μ*	[30]
pAJ2595	*UTP2 URA3 CEN ARS*	[45]
pAJ2596	*utp2-A2D URA3 CEN ARS*	[45]
pAJ2922	*GAL4BD-c-myc-DHR1 TRP1 2μ*	[46]
pAJ2769	*GAL4BD-c-myc-IMP4 TRP1 2μ*	This study.
pAJ3332	*utp2-F149S URA3 CEN ARS*	This study.
pAJ3335	*utp2-L151H URA3 CEN ARS*	This study.
pAJ3347	*utp2-L148S, F149S, L151H URA3 CEN ARS*	This study.

pAJ3348	*utp2-L6P URA3 CEN ARS*	This study.
pAJ3349	*utp2-K7E URA3 CEN ARS*	This study.
pAJ3350	*utp2-L148S URA3 CEN ARS*	This study.
pAJ4093	*utp2-F58S URA3 CEN ARS*	This study.
pAJ4094	*PGAL10-UTP2 LEU2 CEN ARS*	This study.
pAJ4095	*utp2-A2D, L6P, K7E URA3 CEN ARS*	This study.
pAJ4188	*Utp2-GAL4AD-HA LEU2 2µ*	This study.
pAJ4192	*utp2-F58S-GAL4AD-HA LEU2 2µ*	This study.
pAJ4193	*utp2-L148S, F149S, L151H-GAL4AD-HA LEU2 2µ*	This study.
pAJ4194	*utp2-A2D, L6P, K7E-GAL4AD-HA LEU2 2µ*	This study.
pAJ4493	*GAL4BD-c-myc-imp4-V170F TRP1 2µ*	This study.
pAJ4494	*GAL4BD-c-myc-imp4-P252L TRP1 2µ*	This study.
pAJ4503	*GAL4BD-c-myc-DHR1-E360K, E397D, E402G, D408Y TRP1 2µ*	This study.
pAJ4513	*GAL4BD-c-myc-DHR1-R563M, D566Y, E831K, F837L TRP1 2µ*	This study.
pAJ4514	*GAL4BD-c-myc-DHR1-H593Y, R596C, E831K TRP1 2µ*	This study.
pGADT7	*GAL4AD-HA LEU2 2µ*	[89]
pGBKT7	*GAL4BD-c-myc TRP1 2µ*	[89]
pJW1662	*AtIAA17_71-114(AID*)-HA::LEU2 prADH1-OsTIR1*	[80]
pRS416	*URA3 CEN ARS*	[90]

983

984 **Table 3: Oligonucleotide probes used for Northern blotting.**

Target	Sequence
+1-A0	5’ GGTCTCTCTGCTGCCGGAAATG 3’
A0-A1	5’ CCCACCTATTCCCTCTTGC 3’
A2-A3	5’ TGTTACCTCTGGGCCCCGATTG 3’
U3 snoRNA	5’ TAGATTCAATTTCGGTTTCTC 3’

985

986 ## Supporting information

987 Supplemental File 1 – Cumulative list of the suppressors of *bud23*Δ.

988 Supplemental File 2 – Mass spectrometry data for the Enp1-TAP affinity purifications.

989 ## Acknowledgments

990 This work was supported by National Institutes of Health grants GM127127, GM053655,
991 and GM108823 to AWJ, a fellowship from the University of Texas at Austin Graduate School to
992 JJB, and a fellowship from the University of Texas at Austin Office of Undergraduate Research to
993 EWE.

994 We thank S. Baserga and C. Wang for the Imp4 and Bud23 antibodies, respectively. The
995 vector pJW1662 was a gift from J. Weissman (Addgene plasmid #112050). We thank J. Ream and
996 J. Zhu for assistance with cloning, and P. Sujita for assistance with preparing samples for Illumina
997 sequencing submission. We also thank the members of the A. Johnson and Sarinay-Cenik
998 laboratories for helpful comments regarding the manuscript.

999

1000 ## Author contributions

1001 JJB and AWJ conceptualized, analyzed and interpreted data, and wrote the manuscript.
1002 JJB performed experiments and bioinformatic analyses. JJB, RS, EWE, and AWJ isolated and
1003 identified the suppressors of *bud23*Δ.

1004 **References**

1005 1. Ben-Shem A, Garreau de Loubresse N, Melnikov S, Jenner L, Yusupova G, Yusupov M. The
1006 structure of the eukaryotic ribosome at 3.0 Å resolution. Science. 2011;334: 1524–9.
1007 doi:10.1126/science.1212642
1008 2. Sloan KE, Warda AS, Sharma S, Entian K-D, Lafontaine DLJ, Bohnsack MT. Tuning the
1009 ribosome: The influence of rRNA modification on eukaryotic ribosome biogenesis and
1010 function. RNA Biol. Taylor & Francis; 2016;408: 1–16.
1011 doi:10.1080/15476286.2016.1259781
1012 3. Tomecki R, Sikorski PJ, Zakrzewska-Placzek M. Comparison of preribosomal RNA
1013 processing pathways in yeast, plant and human cells - focus on coordinated action of
1014 endo- and exoribonucleases. FEBS Lett. 2017;591: 1801–1850. doi:10.1002/1873-
1015 3468.12682
1016 4. Baßler J, Hurt E. Eukaryotic Ribosome Assembly. Annu Rev Biochem. 2019;88: 281–306.
1017 doi:10.1146/annurev-biochem-013118-110817
1018 5. Klinge S, Woolford JL. Ribosome assembly coming into focus. Nat Rev Mol Cell Biol.
1019 Springer US; 2019;20: 116–131. doi:10.1038/s41580-018-0078-y
1020 6. Chaker-Margot M, Hunziker M, Barandun J, Dill BD, Klinge S. Stage-specific assembly
1021 events of the 6-MDa small-subunit processome initiate eukaryotic ribosome biogenesis.
1022 Nat Struct Mol Biol. Nature Publishing Group; 2015;22: 920–3. doi:10.1038/nsmb.3111
1023 7. Zhang L, Wu C, Cai G, Chen S, Ye K. Stepwise and dynamic assembly of the earliest
1024 precursors of small ribosomal subunits in yeast. Genes Dev. 2016;30: 718–32.
1025 doi:10.1101/gad.274688.115
1026 8. Pérez-Fernández J, Román A, De Las Rivas J, Bustelo XR, Dosil M. The 90S preribosome is
1027 a multimodular structure that is assembled through a hierarchical mechanism. Mol Cell
1028 Biol. 2007;27: 5414–29. doi:10.1128/MCB.00380-07
1029 9. Chen W, Xie Z, Yang F, Ye K. Stepwise assembly of the earliest precursors of large
1030 ribosomal subunits in yeast. Nucleic Acids Res. 2017;45: 6837–6847.
1031 doi:10.1093/nar/gkx254
1032 10. Chaker-Margot M, Klinge S. Assembly and early maturation of large subunit precursors.
1033 RNA. 2019;25: 465–471. doi:10.1261/rna.069799.118
1034 11. Dragon F, Gallagher JEG, Compagnone-Post PA, Mitchell BM, Porwancher KA, Wehner
1035 KA, et al. A large nucleolar U3 ribonucleoprotein required for 18S ribosomal RNA
1036 biogenesis. Nature. 2002;417: 967–70. doi:10.1038/nature00769
1037 12. Grandi P, Rybin V, Bassler J, Petfalski E, Strauss D, Marzioch M, et al. 90S pre-ribosomes
1038 include the 35S pre-rRNA, the U3 snoRNP, and 40S subunit processing factors but
1039 predominantly lack 60S synthesis factors. Mol Cell. 2002;10: 105–15. doi:10.1016/S1097-
1040 2765(02)00579-8
1041 13. Barandun J, Hunziker M, Klinge S. Assembly and structure of the SSU processome-a
1042 nucleolar precursor of the small ribosomal subunit. Curr Opin Struct Biol. Elsevier Ltd;
1043 2018;49: 85–93. doi:10.1016/j.sbi.2018.01.008
1044 14. Chaker-Margot M. Assembly of the small ribosomal subunit in yeast: mechanism and
1045 regulation. RNA. 2018;24: 881–891. doi:10.1261/rna.066985.118

1046 15. Barandun J, Chaker-Margot M, Hunziker M, Molloy KR, Chait BT, Klinge S. The complete
1047 structure of the small-subunit processome. Nat Struct Mol Biol. Nature Publishing Group;
1048 2017; 1–36. doi:10.1038/nsmb.3472
1049 16. Cheng J, Kellner N, Berninghausen O, Hurt E, Beckmann R. 3.2-Å-resolution structure of
1050 the 90S preribosome before A1 pre-rRNA cleavage. Nat Struct Mol Biol. Nature
1051 Publishing Group; 2017;24: 954–964. doi:10.1038/nsmb.3476
1052 17. Sun Q, Zhu X, Qi J, An W, Lan P, Tan D, et al. Molecular architecture of the 90S small
1053 subunit pre-ribosome. Elife. 2017;6: e22086. doi:10.7554/eLife.22086
1054 18. Hunziker M, Barandun J, Buzovetsky O, Steckler C, Molina H, Klinge S. Conformational
1055 switches control early maturation of the eukaryotic small ribosomal subunit. Elife.
1056 2019;8: 1–16. doi:10.7554/eLife.45185
1057 19. Cheng J, Baßler J, Fischer P, Lau B, Kellner N, Kunze R, et al. Thermophile 90S Pre-
1058 ribosome Structures Reveal the Reverse Order of Co-transcriptional 18S rRNA Subdomain
1059 Integration. Mol Cell. 2019; 1–14. doi:10.1016/j.molcel.2019.06.032
1060 20. Schäfer T, Strauss D, Petfalski E, Tollervey D, Hurt E. The path from nucleolar 90S to
1061 cytoplasmic 40S pre-ribosomes. EMBO J. 2003;22: 1370–80. doi:10.1093/emboj/cdg121
1062 21. Hunziker M, Barandun J, Petfalski E, Tan D, Delan-Forino C, Molloy KR, et al. UtpA and
1063 UtpB chaperone nascent pre-ribosomal RNA and U3 snoRNA to initiate eukaryotic
1064 ribosome assembly. Nat Commun. 2016;7: 12090. doi:10.1038/ncomms12090
1065 22. Beltrame M, Henry Y, Tollervey D. Mutational analysis of an essential binding site for the
1066 U3 snoRNA in the 5' external transcribed spacer of yeast pre-rRNA. Nucleic Acids Res.
1067 1994;22: 4057–65. doi:10.1093/nar/22.20.4057
1068 23. Beltrame M, Tollervey D. Base pairing between U3 and the pre-ribosomal RNA is required
1069 for 18S rRNA synthesis. EMBO J. 1995;14: 4350–6. doi:10.1002/j.1460-
1070 2075.1995.tb00109.x
1071 24. Sharma K, Tollervey D. Base pairing between U3 small nucleolar RNA and the 5' end of
1072 18S rRNA is required for pre-rRNA processing. Mol Cell Biol. 1999;19: 6012–9.
1073 doi:10.1128/mcb.19.9.6012
1074 25. Dutca LM, Gallagher JEG, Baserga SJ. The initial U3 snoRNA:pre-rRNA base pairing
1075 interaction required for pre-18S rRNA folding revealed by in vivo chemical probing.
1076 Nucleic Acids Res. 2011;39: 5164–80. doi:10.1093/nar/gkr044
1077 26. Marmier-Gourrier N, Cléry A, Schlotter F, Senty-Ségault V, Branlant C. A second base pair
1078 interaction between U3 small nucleolar RNA and the 5'-ETS region is required for early
1079 cleavage of the yeast pre-ribosomal RNA. Nucleic Acids Res. 2011;39: 9731–45.
1080 doi:10.1093/nar/gkr675
1081 27. Petrov AS, Bernier CR, Gulen B, Waterbury CC, Hershkovits E, Hsiao C, et al. Secondary
1082 structures of rRNAs from all three domains of life. PLoS One. 2014;9: e88222.
1083 doi:10.1371/journal.pone.0088222
1084 28. Kressler D, Hurt E, Baßler J. A Puzzle of Life: Crafting Ribosomal Subunits. Trends Biochem
1085 Sci. 2017;42: 640–654. doi:10.1016/j.tibs.2017.05.005
1086 29. Sardana R, Liu X, Granneman S, Zhu J, Gill M, Papoulas O, et al. The DEAH-box helicase
1087 Dhr1 dissociates U3 from the pre-rRNA to promote formation of the central pseudoknot.
1088 PLoS Biol. 2015;13: e1002083. doi:10.1371/journal.pbio.1002083
1089 30. Zhu J, Liu X, Anjos M, Correll CC, Johnson AW. Utp14 Recruits and Activates the RNA

1090 Helicase Dhr1 To Undock U3 snoRNA from the Preribosome. Mol Cell Biol. 2016;36: 965–
1091 78. doi:10.1128/MCB.00773-15
1092 31. Roychowdhury A, Joret C, Bourgeois G, Heurgué-Hamard V, Lafontaine DLJ, Graille M.
1093 The DEAH-box RNA helicase Dhr1 contains a remarkable carboxyl terminal domain
1094 essential for small ribosomal subunit biogenesis. Nucleic Acids Res. 2019;
1095 doi:10.1093/nar/gkz529
1096 32. Boneberg FM, Brandmann T, Kobel L, van den Heuvel J, Bargsten K, Bammert L, et al.
1097 Molecular mechanism of the RNA helicase DHX37 and its activation by UTP14A in
1098 ribosome biogenesis. RNA. 2019;25: 685–701. doi:10.1261/rna.069609.118
1099 33. Black JJ, Wang Z, Goering LM, Johnson AW. Utp14 interaction with the Small Subunit
1100 Processome. RNA. 2018; rna.066373.118. doi:10.1261/rna.066373.118
1101 34. Colley A, Beggs JD, Tollervey D, Lafontaine DL. Dhr1p, a putative DEAH-box RNA helicase,
1102 is associated with the box C+D snoRNP U3. Mol Cell Biol. 2000;20: 7238–46.
1103 doi:10.1128/mcb.20.19.7238-7246.2000
1104 35. Granneman S, Bernstein KA, Bleichert F, Baserga SJ. Comprehensive mutational analysis
1105 of yeast DEXD/H box RNA helicases required for small ribosomal subunit synthesis. Mol
1106 Cell Biol. 2006;26: 1183–94. doi:10.1128/MCB.26.4.1183-1194.2006
1107 36. Bleichert F, Granneman S, Osheim YN, Beyer AL, Baserga SJ. The PINc domain protein
1108 Utp24, a putative nuclease, is required for the early cleavage steps in 18S rRNA
1109 maturation. Proc Natl Acad Sci U S A. 2006;103: 9464–9. doi:10.1073/pnas.0603673103
1110 37. Wells GR, Weichmann F, Colvin D, Sloan KE, Kudla G, Tollervey D, et al. The PIN domain
1111 endonuclease Utp24 cleaves pre-ribosomal RNA at two coupled sites in yeast and
1112 humans. Nucleic Acids Res. 2016; gkw213. doi:10.1093/nar/gkw213
1113 38. An W, Du Y, Ye K. Structural and functional analysis of Utp24, an endonuclease for
1114 processing 18S ribosomal RNA. PLoS One. 2018;13: e0195723.
1115 doi:10.1371/journal.pone.0195723
1116 39. White J, Li Z, Sardana R, Bujnicki JM, Marcotte EM, Johnson AW. Bud23 methylates
1117 G1575 of 18S rRNA and is required for efficient nuclear export of pre-40S subunits. Mol
1118 Cell Biol. 2008;28: 3151–61. doi:10.1128/MCB.01674-07
1119 40. Létoquart J, Huvelle E, Wacheul L, Bourgeois G, Zorbas C, Graille M, et al. Structural and
1120 functional studies of Bud23-Trm112 reveal 18S rRNA N7-G1575 methylation occurs on
1121 late 40S precursor ribosomes. Proc Natl Acad Sci U S A. 2014;111: E5518-26.
1122 doi:10.1073/pnas.1413089111
1123 41. Sardana R, Johnson AW. The methyltransferase adaptor protein Trm112 is involved in
1124 biogenesis of both ribosomal subunits. Mol Biol Cell. 2012;23: 4313–22.
1125 doi:10.1091/mbc.E12-05-0370
1126 42. Figaro S, Wacheul L, Schillewaert S, Graille M, Huvelle E, Mongeard R, et al. Trm112 Is
1127 Required for Bud23-Mediated Methylation of the 18S rRNA at Position G1575. Mol Cell
1128 Biol. 2012;32: 2254–2267. doi:10.1128/MCB.06623-11
1129 43. Lin J-L, Yu H-C, Chao J-L, Wang C, Cheng M-Y. New phenotypes generated by the G57R
1130 mutation of BUD23 in Saccharomyces cerevisiae. Yeast. 2012;29: 537–546.
1131 doi:10.1002/yea.2934
1132 44. Ameismeier M, Cheng J, Berninghausen O, Beckmann R. Visualizing late states of human
1133 40S ribosomal subunit maturation. Nature. 2018;558: 249–253. doi:10.1038/s41586-018-

1134 0193-0
1135 45. Sardana R, White JP, Johnson AW. The rRNA methyltransferase Bud23 shows functional
1136 interaction with components of the SSU processome and RNase MRP. RNA. 2013;19:
1137 828–40. doi:10.1261/rna.037671.112
1138 46. Sardana R, Zhu J, Gill M, Johnson AW. Physical and functional interaction between the
1139 methyltransferase Bud23 and the essential DEAH-box RNA helicase Ecm16. Mol Cell Biol.
1140 2014;34: 2208–20. doi:10.1128/MCB.01656-13
1141 47. Sardana R. From knobs to a central pseudoknot: understanding 40S ribosomal subunit
1142 biogenesis through Bud23. The University of Texas at Austin. 2013.
1143 48. Lee SJ, Baserga SJ. Imp3p and Imp4p, two specific components of the U3 small nucleolar
1144 ribonucleoprotein that are essential for pre-18S rRNA processing. Mol Cell Biol. 1999;19:
1145 5441–52. doi:10.1128/MCB.19.8.5441
1146 49. Dunbar DA, Wormsley S, Agentis TM, Baserga SJ. Mpp10p, a U3 small nucleolar
1147 ribonucleoprotein component required for pre-18S rRNA processing in yeast. Mol Cell
1148 Biol. 1997;17: 5803–12. doi:10.1128/mcb.17.10.5803
1149 50. Lee SJ, Baserga SJ. Functional separation of pre-rRNA processing steps revealed by
1150 truncation of the U3 small nucleolar ribonucleoprotein component, Mpp10. Proc Natl
1151 Acad Sci U S A. 1997;94: 13536–41. doi:10.1073/pnas.94.25.13536
1152 51. Gallagher JEG, Baserga SJ. Two-hybrid Mpp10p interaction-defective Imp4 proteins are
1153 not interaction defective in vivo but do confer specific pre-rRNA processing defects in
1154 *Saccharomyces cerevisiae*. Nucleic Acids Res. 2004;32: 1404–13. doi:10.1093/nar/gkh318
1155 52. Wehner KA, Gallagher JEG, Baserga SJ. Components of an interdependent unit within the
1156 SSU processome regulate and mediate its activity. Mol Cell Biol. 2002;22: 7258–67.
1157 doi:10.1128/MCB.22.20.7258-7267.2002
1158 53. Sá-Moura B, Kornprobst M, Kharde S, Ahmed YL, Stier G, Kunze R, et al. Mpp10
1159 represents a platform for the interaction of multiple factors within the 90S pre-ribosome.
1160 PLoS One. 2017;12: e0183272. doi:10.1371/journal.pone.0183272
1161 54. Baßler J, Ahmed YL, Kallas M, Kornprobst M, Calviño FR, Gnädig M, et al. Interaction
1162 network of the ribosome assembly machinery from a eukaryotic thermophile. Protein
1163 Sci. 2016;22: 1–50. doi:10.1002/pro.3085
1164 55. Vincent NG, Charette JM, Baserga SJ. The SSU processome interactome in *Saccharomyces*
1165 *cerevisiae* reveals novel protein subcomplexes. RNA. 2018;24: 77–89.
1166 doi:10.1261/rna.062927.117
1167 56. Liu PC, Thiele DJ. Novel stress-responsive genes EMG1 and NOP14 encode conserved,
1168 interacting proteins required for 40S ribosome biogenesis. Mol Biol Cell. 2001;12: 3644–
1169 57. doi:10.1091/mbc.12.11.3644
1170 57. Wegierski T, Billy E, Nasr F, Filipowicz W. Bms1p, a G-domain-containing protein,
1171 associates with Rcl1p and is required for 18S rRNA biogenesis in yeast. RNA. 2001;7:
1172 1254–67. doi:10.1017/S1355838201012079
1173 58. Gelperin D, Horton L, Beckman J, Hensold J, Lemmon SK. Bms1p, a novel GTP-binding
1174 protein, and the related Tsr1p are required for distinct steps of 40S ribosome biogenesis
1175 in yeast. RNA. 2001;7: 1268–83. doi:10.1017/S1355838201013073
1176 59. Karbstein K, Doudna JA. GTP-dependent formation of a ribonucleoprotein subcomplex
1177 required for ribosome biogenesis. J Mol Biol. 2006;356: 432–43.

1178 doi:10.1016/j.jmb.2005.11.052
1179 60. Karbstein K, Jonas S, Doudna JA. An essential GTPase promotes assembly of preribosomal
1180 RNA processing complexes. Mol Cell. 2005;20: 633–43. doi:10.1016/j.molcel.2005.09.017
1181 61. Delprato A, Al Kadri Y, Pérébaskine N, Monfoulet C, Henry Y, Henras AK, et al. Crucial role
1182 of the Rcl1p-Bms1p interaction for yeast pre-ribosomal RNA processing. Nucleic Acids
1183 Res. 2014;42: 10161–72. doi:10.1093/nar/gku682
1184 62. Wittinghofer A, Vetter IR. Structure-function relationships of the G domain, a canonical
1185 switch motif. Annu Rev Biochem. 2011;80: 943–71. doi:10.1146/annurev-biochem-
1186 062708-134043
1187 63. Nissen P, Thirup S, Kjeldgaard M, Nyborg J. The crystal structure of Cys-tRNACys-EF-Tu-
1188 GDPNP reveals general and specific features in the ternary complex and in tRNA.
1189 Structure. 1999;7: 143–56.
1190 64. Song H, Parsons MR, Rowsell S, Leonard G, Phillips SEV. Crystal structure of intact
1191 elongation factor EF-Tu from Escherichia coli in GDP conformation at 2.05 A resolution. J
1192 Mol Biol. 1999;285: 1245–56. doi:10.1006/jmbi.1998.2387
1193 65. Choudhury P, Hackert P, Memet I, Sloan KE, Bohnsack MT. The human RNA helicase
1194 DHX37 is required for release of the U3 snoRNP from pre-ribosomal particles. RNA Biol.
1195 Taylor & Francis; 2018;00: 1–15. doi:10.1080/15476286.2018.1556149
1196 66. Nishimura K, Fukagawa T, Takisawa H, Kakimoto T, Kanemaki M. An auxin-based degron
1197 system for the rapid depletion of proteins in nonplant cells. Nat Methods. Nature
1198 Publishing Group; 2009;6: 917–22. doi:10.1038/nmeth.1401
1199 67. Gérczei T, Correll CC. Imp3p and Imp4p mediate formation of essential U3-precursor
1200 rRNA (pre-rRNA) duplexes, possibly to recruit the small subunit processome to the pre-
1201 rRNA. Proc Natl Acad Sci U S A. 2004;101: 15301–6. doi:10.1073/pnas.0406819101
1202 68. Lackmann F, Belikov S, Burlacu E, Granneman S, Wieslander L. Maturation of the 90S pre-
1203 ribosome requires Mrd1 dependent U3 snoRNA and 35S pre-rRNA structural
1204 rearrangements. Nucleic Acids Res. Oxford University Press; 2018;46: 3692–3706.
1205 doi:10.1093/nar/gky036
1206 69. Fischer U, Schäuble N, Schütz S, Altvater M, Chang Y, Faza MB, et al. A non-canonical
1207 mechanism for Crm1-export cargo complex assembly. Elife. 2015;4: 1–20.
1208 doi:10.7554/eLife.05745
1209 70. Ferreira-Cerca S, Kiburu I, Thomson E, LaRonde N, Hurt E. Dominant Rio1 kinase/ATPase
1210 catalytic mutant induces trapping of late pre-40S biogenesis factors in 80S-like
1211 ribosomes. Nucleic Acids Res. 2014;42: 8635–47. doi:10.1093/nar/gku542
1212 71. Parker MD, Collins JC, Korona B, Ghalei H, Karbstein K. A kinase-dependent checkpoint
1213 prevents escape of immature ribosomes into the translating pool. Gilbert W V, editor.
1214 PLOS Biol. 2019;17: e3000329. doi:10.1371/journal.pbio.3000329
1215 72. Zorbas C, Nicolas E, Wacheul L, Huvelle E, Heurgué-Hamard V, Lafontaine DLJ. The human
1216 18S rRNA base methyltransferases DIMT1L and WBSCR22-TRMT112 but not rRNA
1217 modification are required for ribosome biogenesis. Mol Biol Cell. 2015;26: 2080–95.
1218 doi:10.1091/mbc.E15-02-0073
1219 73. Õunap K, Käsper L, Kurg A, Kurg R. The human WBSCR22 protein is involved in the
1220 biogenesis of the 40S ribosomal subunits in mammalian cells. Wieden H-J, editor. PLoS
1221 One. 2013;8: e75686. doi:10.1371/journal.pone.0075686

1222 74. Haag S, Kretschmer J, Bohnsack MT. WBSCR22/Merm1 is required for late nuclear pre-
1223 ribosomal RNA processing and mediates N7-methylation of G1639 in human 18S rRNA.
1224 RNA. 2015;21: 180–7. doi:10.1261/rna.047910.114
1225 75. Small EC, Leggett SR, Winans AA, Staley JP. The EF-G-like GTPase Snu114p regulates
1226 spliceosome dynamics mediated by Brr2p, a DExD/H box ATPase. Mol Cell. 2006;23: 389–
1227 99. doi:10.1016/j.molcel.2006.05.043
1228 76. Koodathingal P, Staley JP. Splicing fidelity. RNA Biol. 2013;10: 1073–1079.
1229 doi:10.4161/rna.25245
1230 77. Yang F, Wang X-Y, Zhang Z-M, Pu J, Fan Y-J, Zhou J, et al. Splicing proofreading at 5' splice
1231 sites by ATPase Prp28p. Nucleic Acids Res. 2013;41: 4660–70. doi:10.1093/nar/gkt149
1232 78. Tong AHY, Evangelista M, Parsons AB, Xu H, Bader GD, Pagé N, et al. Systematic genetic
1233 analysis with ordered arrays of yeast deletion mutants. Science. 2001;294: 2364–8.
1234 doi:10.1126/science.1065810
1235 79. Winzeler EA, Shoemaker DD, Astromoff A, Liang H, Anderson K, Andre B, et al. Functional
1236 characterization of the *S. cerevisiae* genome by gene deletion and parallel analysis.
1237 Science. 1999;285: 901–6. doi:10.1126/science.285.5429.901
1238 80. Costa EA, Subramanian K, Nunnari J, Weissman JS. Defining the physiological role of SRP
1239 in protein-targeting efficiency and specificity. Science. 2018;359: 689–692.
1240 doi:10.1126/science.aar3607
1241 81. Langmead B, Salzberg SL. Fast gapped-read alignment with Bowtie 2. Nat Methods.
1242 2012;9: 357–9. doi:10.1038/nmeth.1923
1243 82. Li H, Handsaker B, Wysoker A, Fennell T, Ruan J, Homer N, et al. The Sequence
1244 Alignment/Map format and SAMtools. Bioinformatics. 2009;25: 2078–9.
1245 doi:10.1093/bioinformatics/btp352
1246 83. Narasimhan V, Danecek P, Scally A, Xue Y, Tyler-Smith C, Durbin R. BCFtools/RoH: a
1247 hidden Markov model approach for detecting autozygosity from next-generation
1248 sequencing data. Bioinformatics. 2016;32: 1749–51. doi:10.1093/bioinformatics/btw044
1249 84. Danecek P, Auton A, Abecasis G, Albers CA, Banks E, DePristo MA, et al. The variant call
1250 format and VCFtools. Bioinformatics. 2011;27: 2156–8.
1251 doi:10.1093/bioinformatics/btr330
1252 85. Oeffinger M, Wei KE, Rogers R, DeGrasse JA, Chait BT, Aitchison JD, et al. Comprehensive
1253 analysis of diverse ribonucleoprotein complexes. Nat Methods. 2007;4: 951–6.
1254 doi:10.1038/nmeth1101
1255 86. Musalgaonkar S, Black JJ, Johnson A. The L1 stalk is required for efficient export of
1256 nascent large ribosomal subunits in yeast. RNA. 2019; rna.071811.119.
1257 doi:10.1261/rna.071811.119
1258 87. Ghaemmaghami S, Huh W-K, Bower K, Howson RW, Belle a, Dephoure N, et al. Global
1259 analysis of protein expression in yeast. Nature. 2003;425: 737–741.
1260 doi:10.1038/nature02046\nnature02046 [pii]
1261 88. James P, Halladay J, Craig E a. Genomic libraries and a host strain designed for highly
1262 efficient two-hybrid selection in yeast. Genetics. 1996;144: 1425–36.
1263 89. Patel SS, Belmont BJ, Sante JM, Rexach MF. Natively unfolded nucleoporins gate protein
1264 diffusion across the nuclear pore complex. Cell. 2007;129: 83–96.
1265 doi:10.1016/j.cell.2007.01.044

1266 90. Sikorski RS, Hieter P. A system of shuttle vectors and yeast host strains designed for
1267 efficient manipulation of DNA in *Saccharomyces cerevisiae*. Genetics. 1989;122: 19–27.
1268 doi:0378111995000377 [pii]
1269

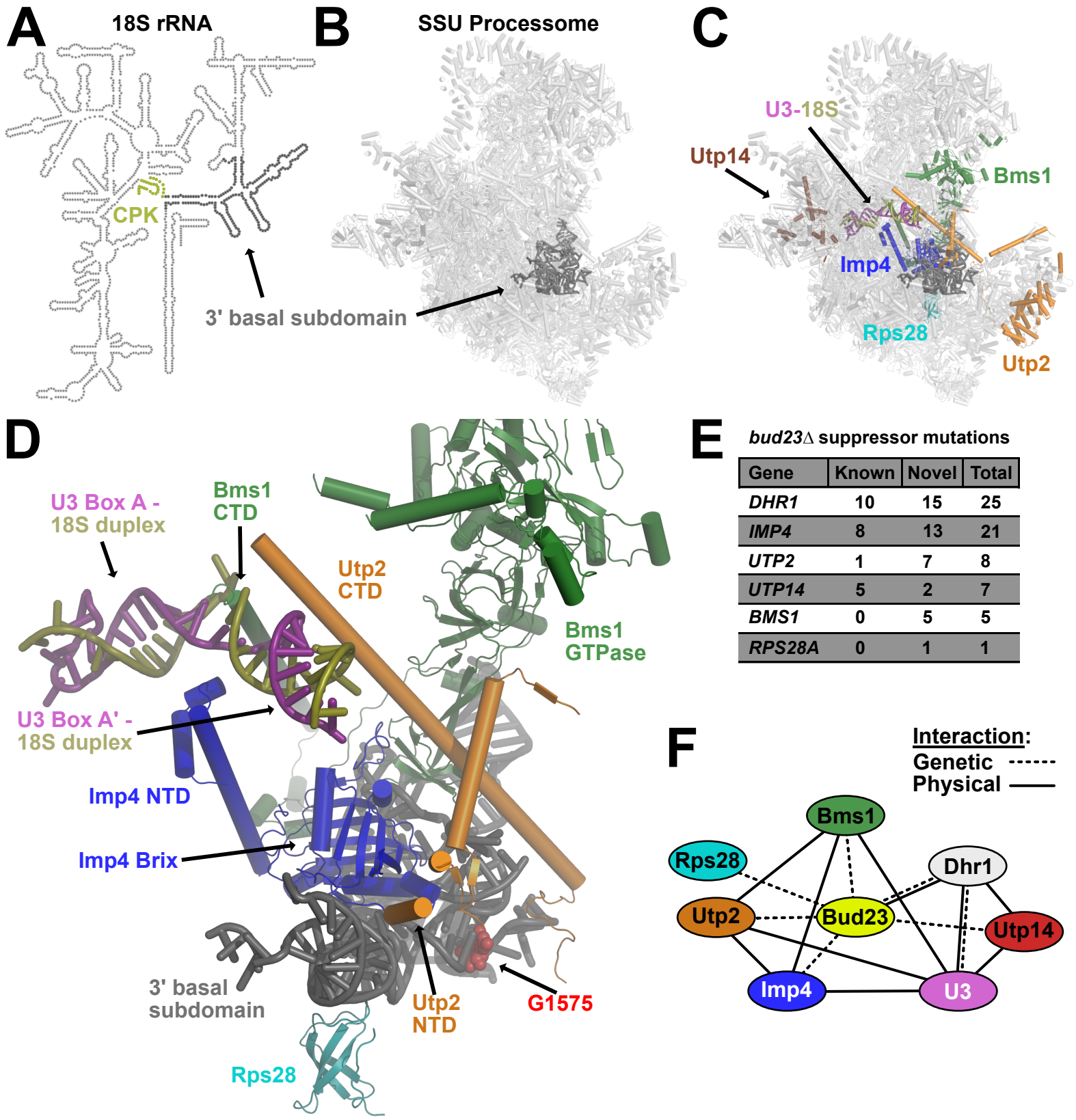

***bud23*Δ suppressor mutations**

Gene	Known	Novel	Total
DHR1	10	15	25
IMP4	8	13	21
UTP2	1	7	8
UTP14	5	2	7
BMS1	0	5	5
RPS28A	0	1	1

Figure 1, Black, et al 2020

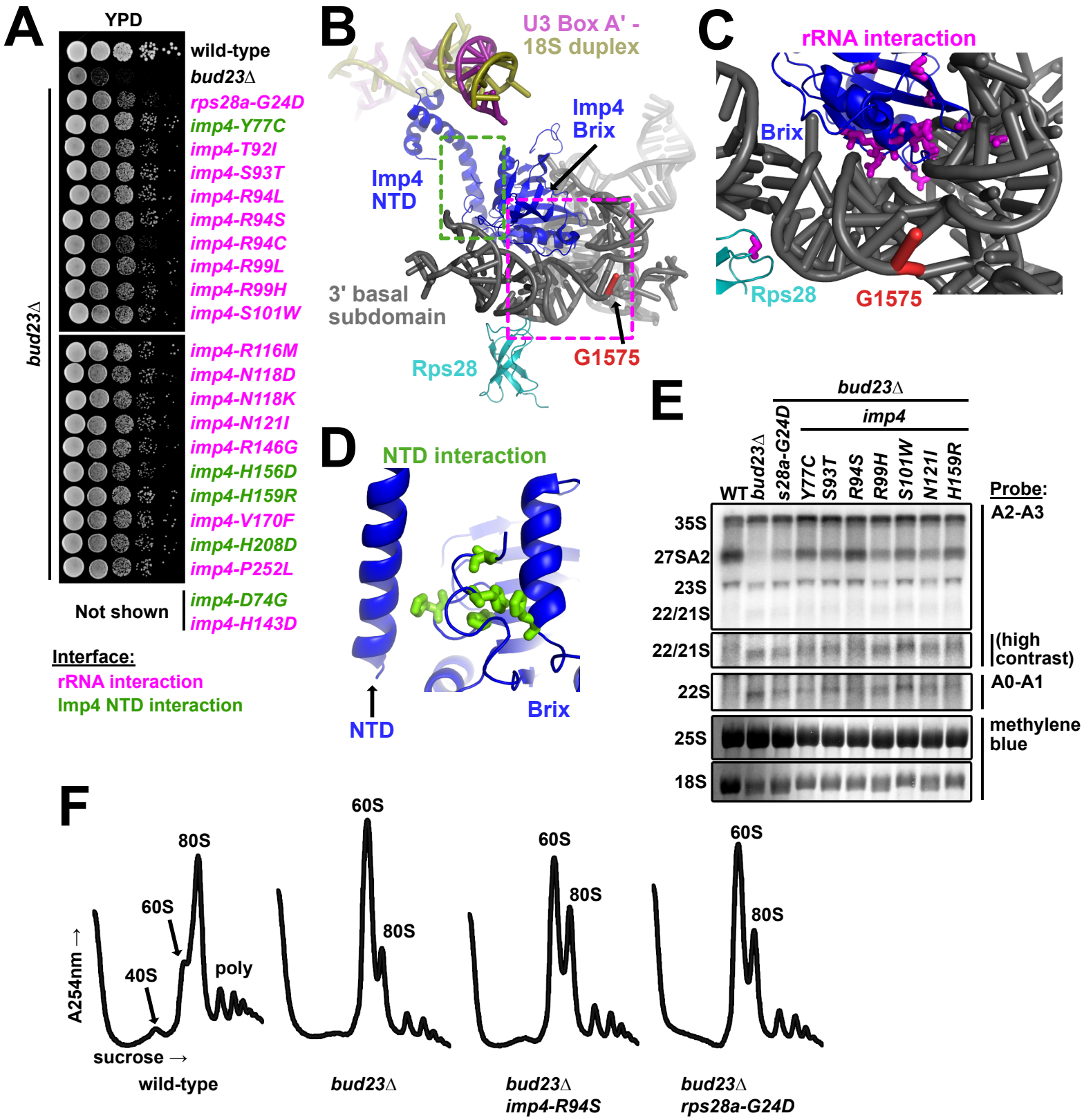

Figure 2, Black, et al 2020

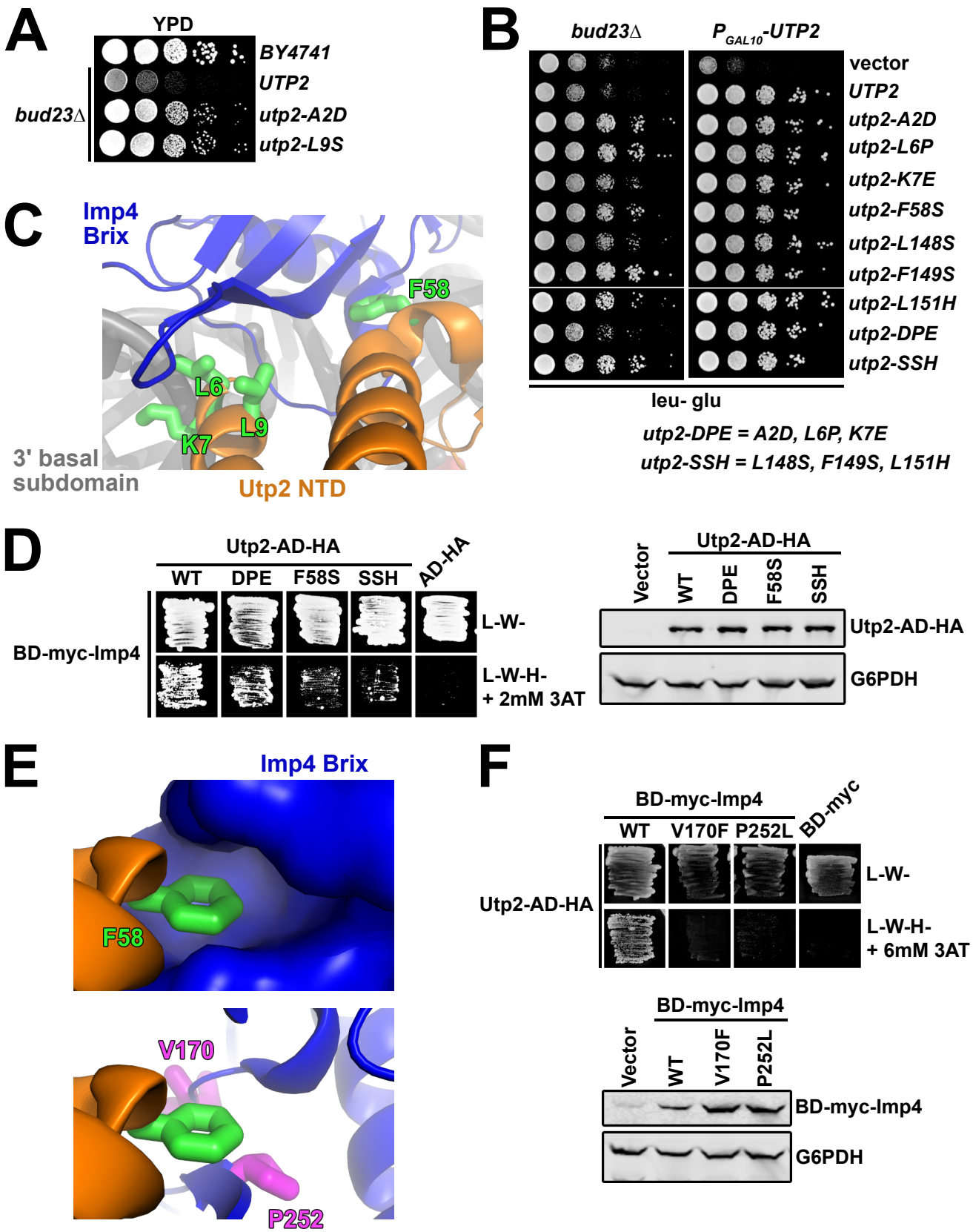

Figure 3, Black, et al 2020

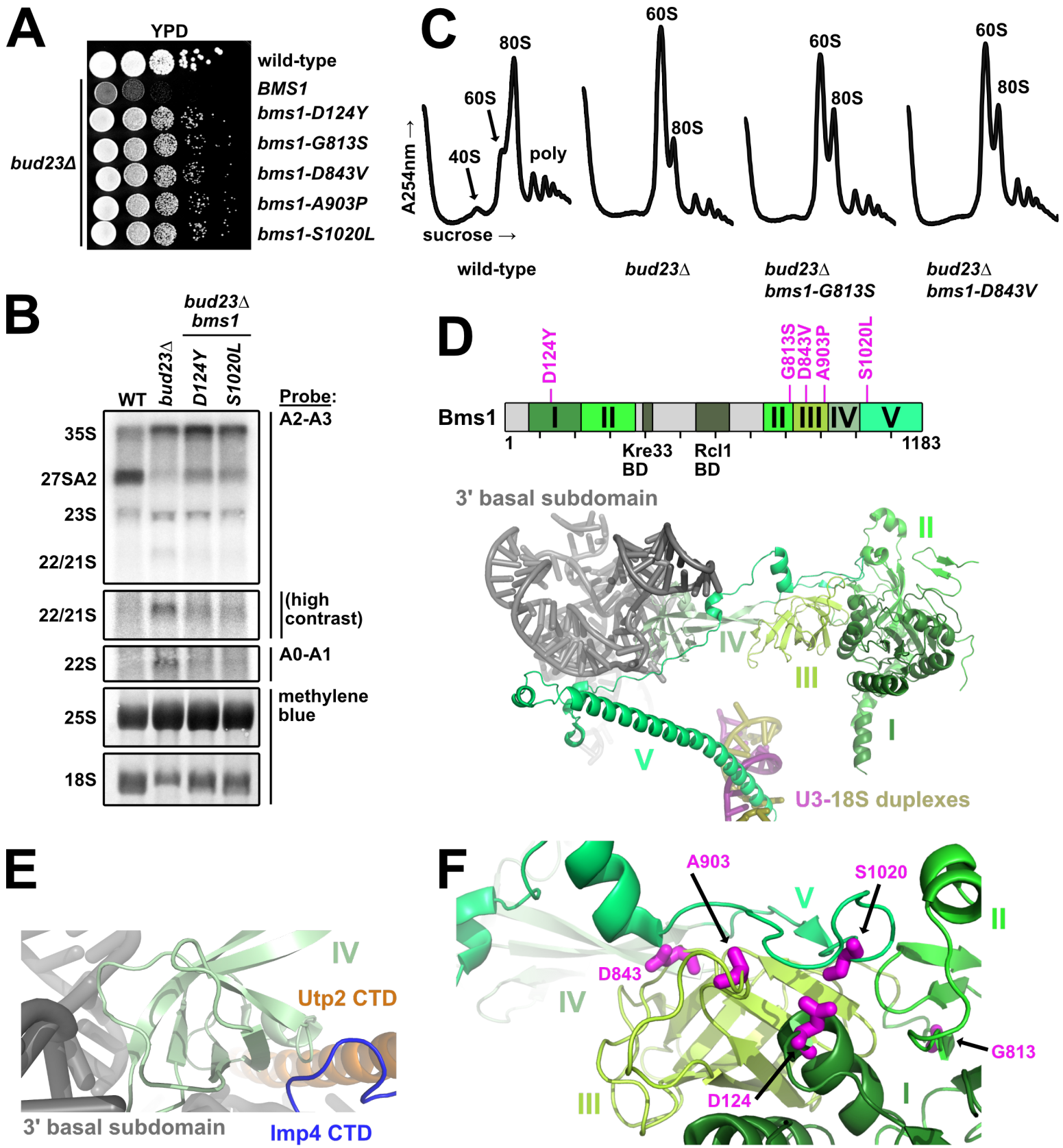

Figure 4, Black, et al 2020

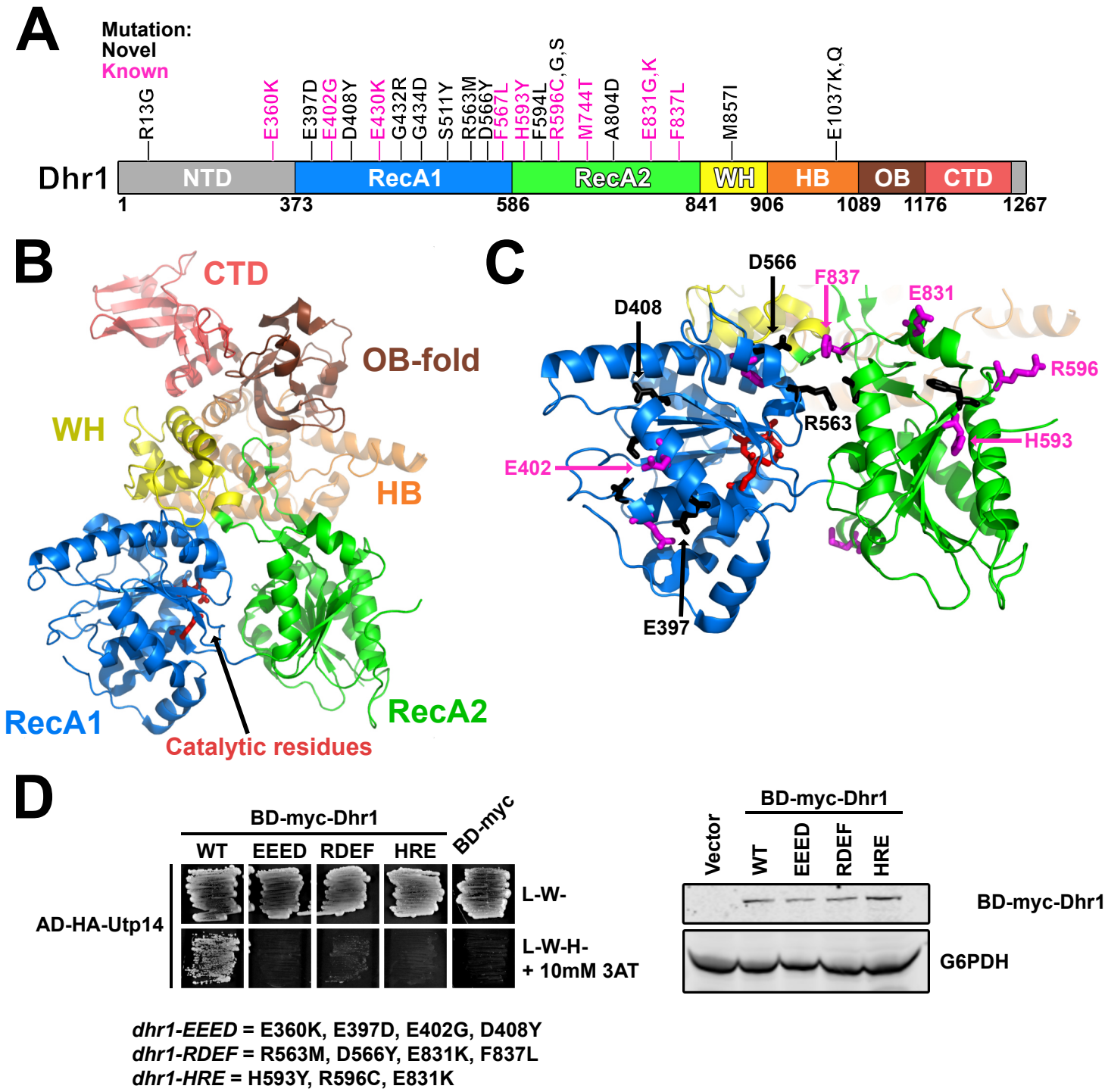

Figure 5, Black, et al 2020

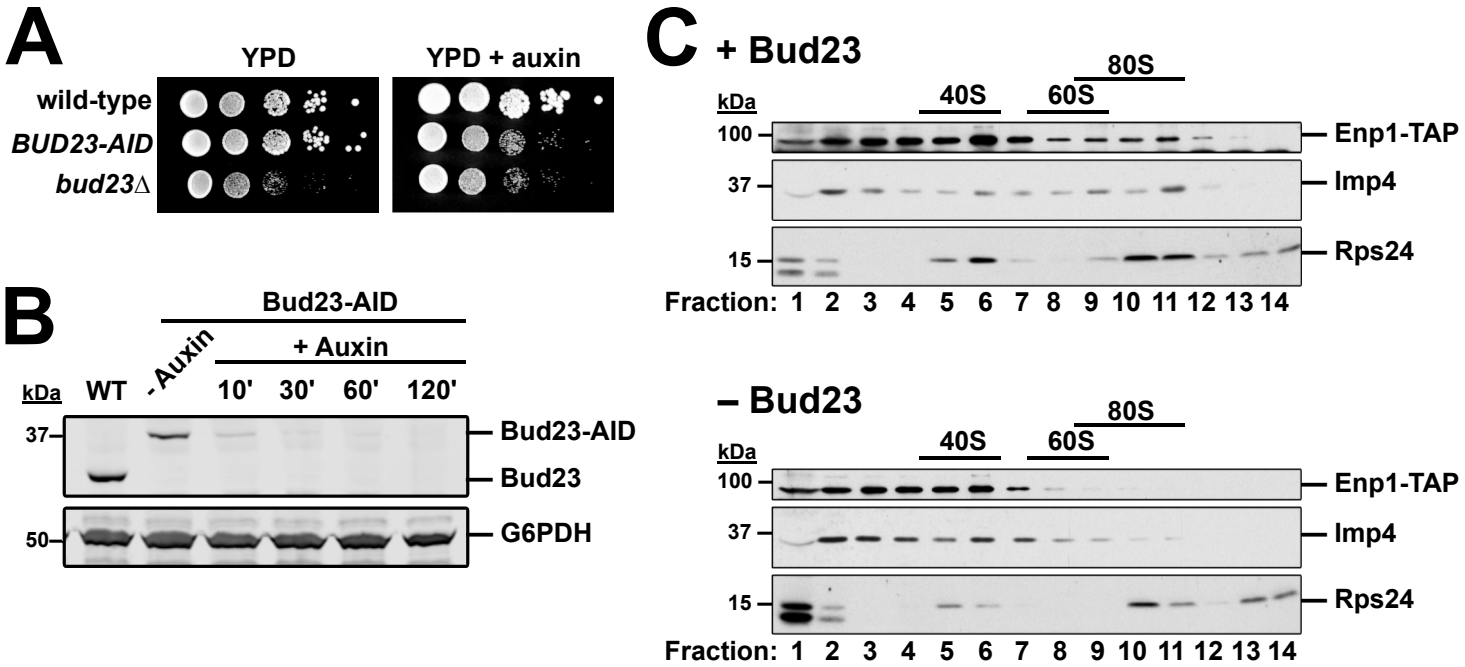

Figure 6, Black, et al 2020

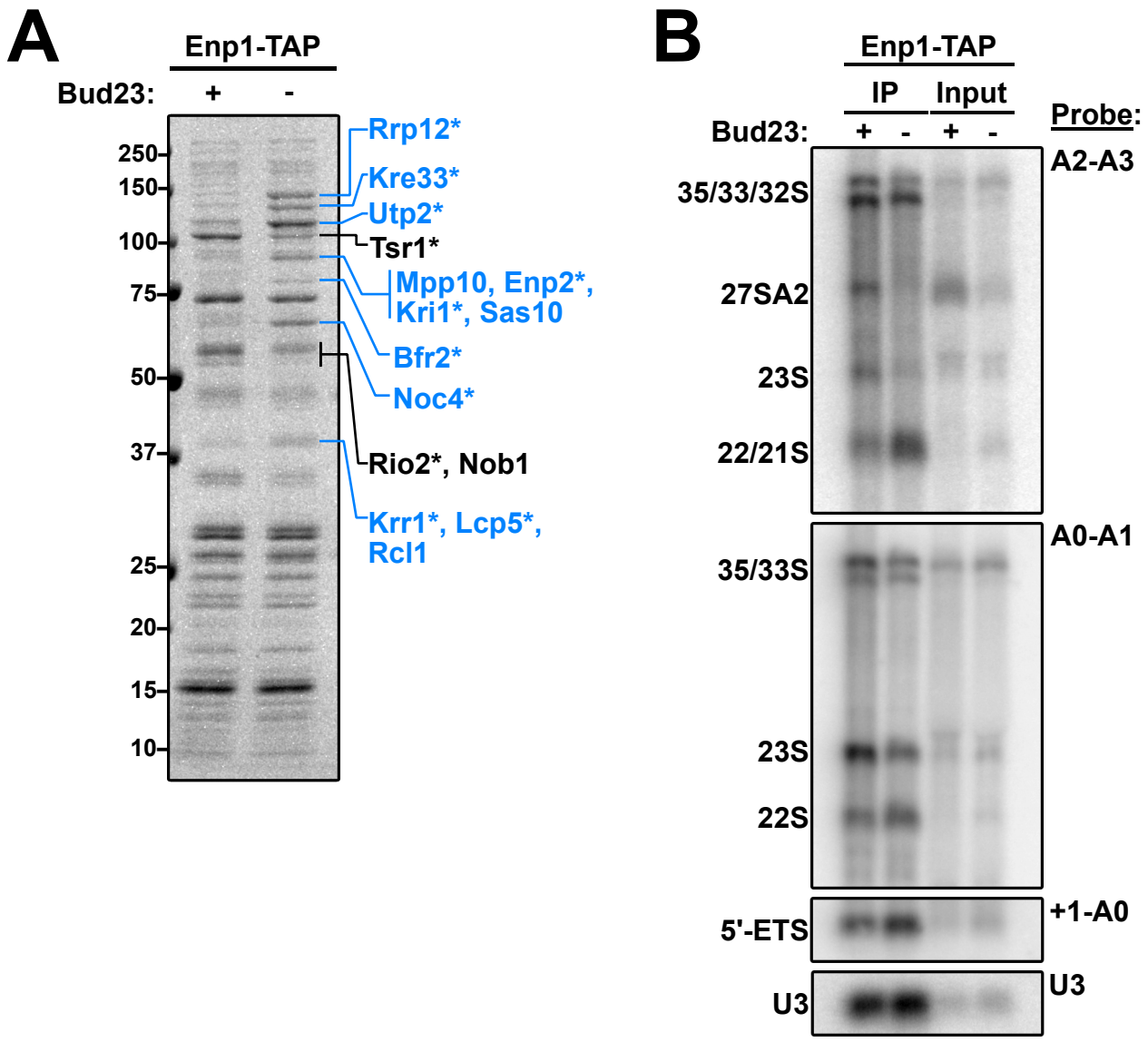

Figure 7, Black, et al 2020

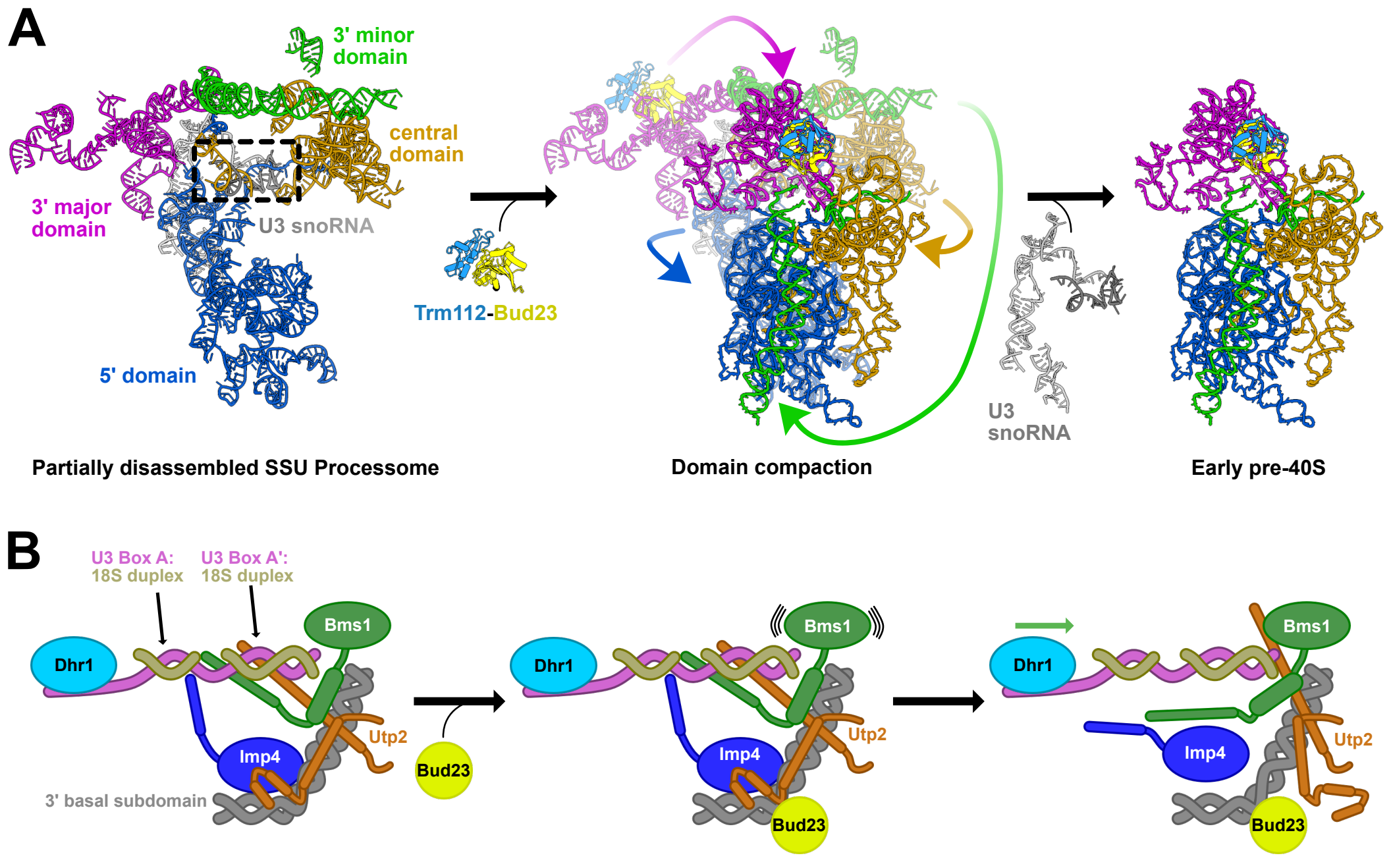

Figure 8, Black, et al 2020

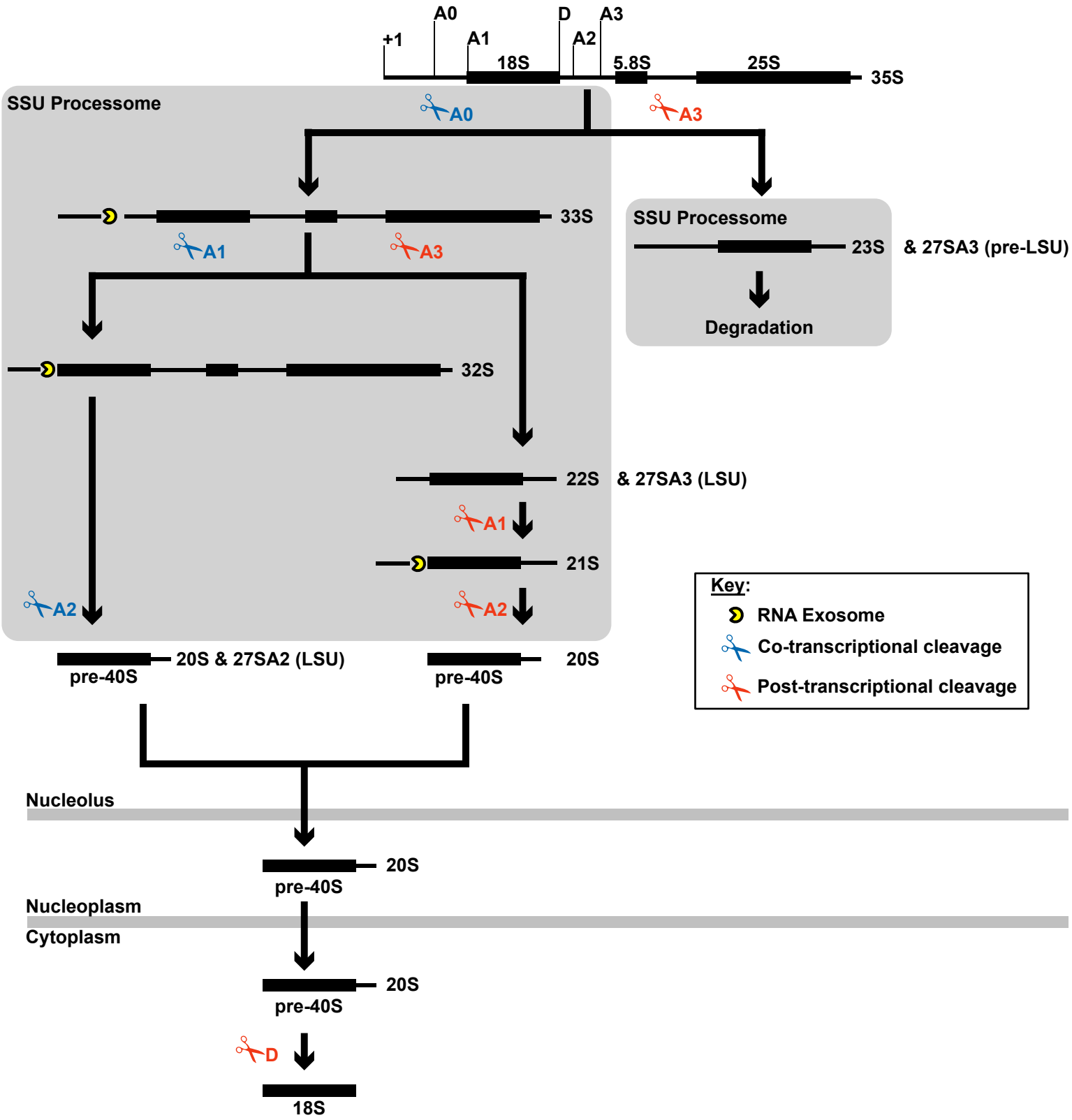

Figure S1, Black, et al 2020

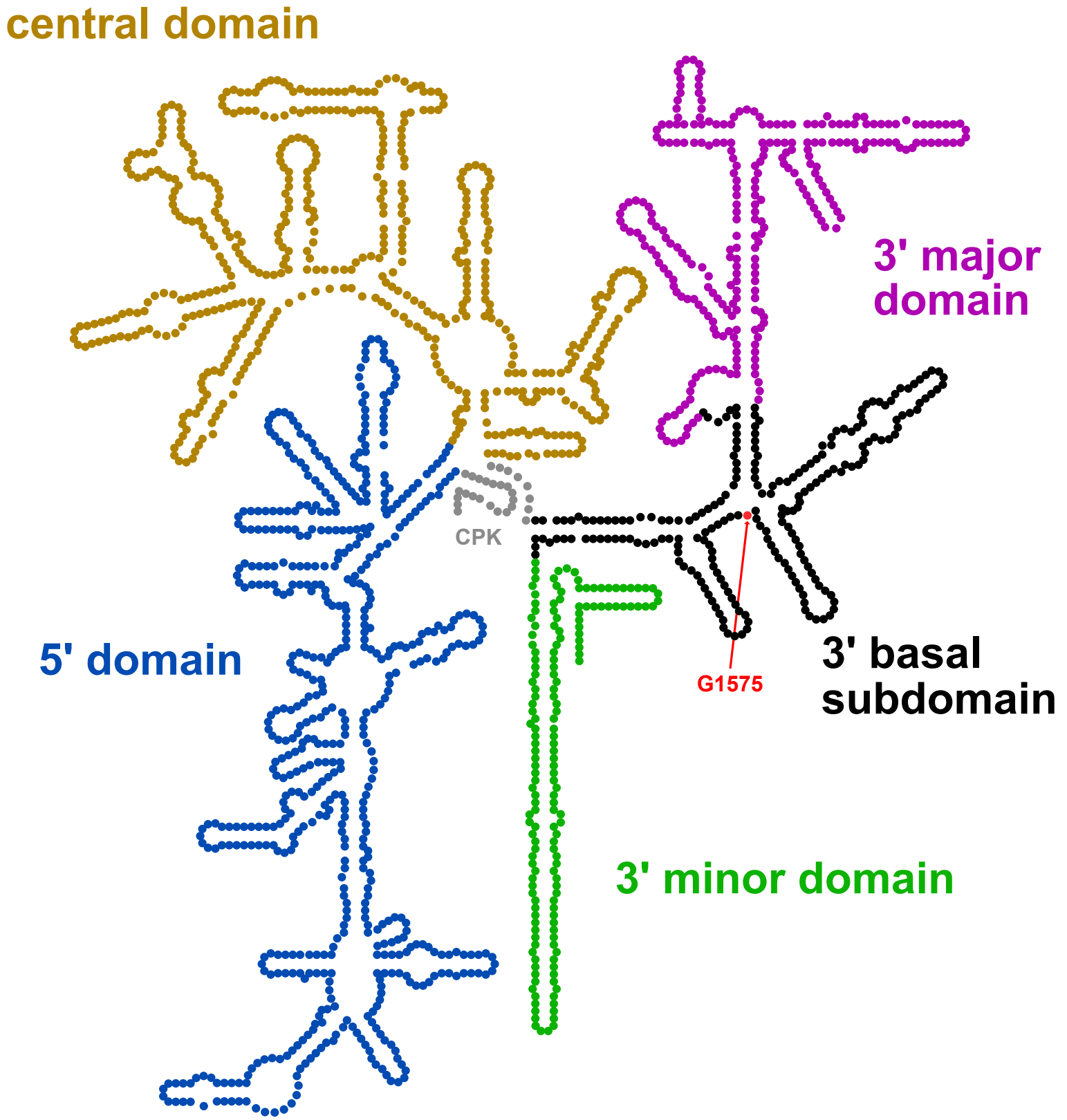

A 3D-based secondary structure, generated by RiboVision.

Figure S2, Black, et al 2020

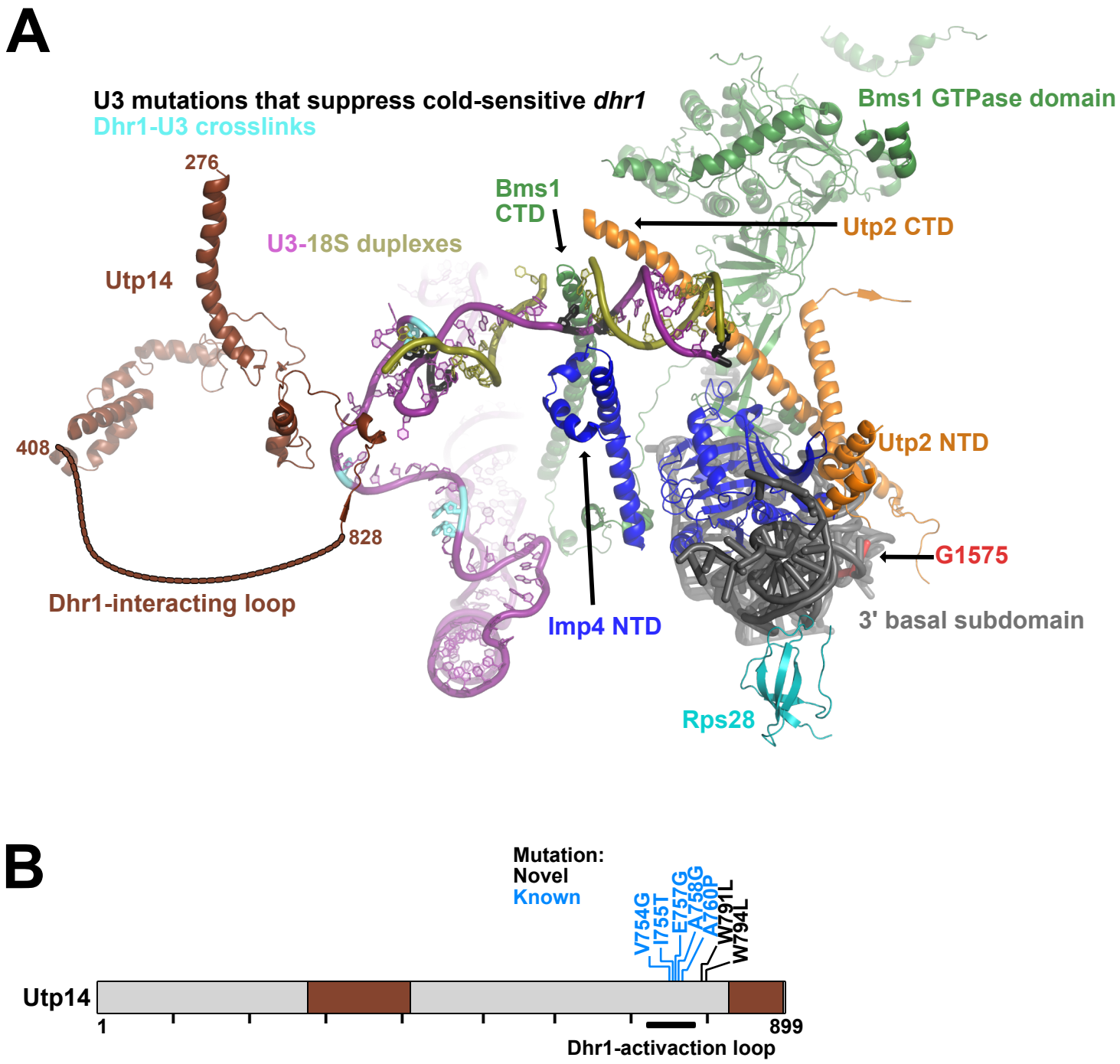

Figure S3, Black, et al 2020

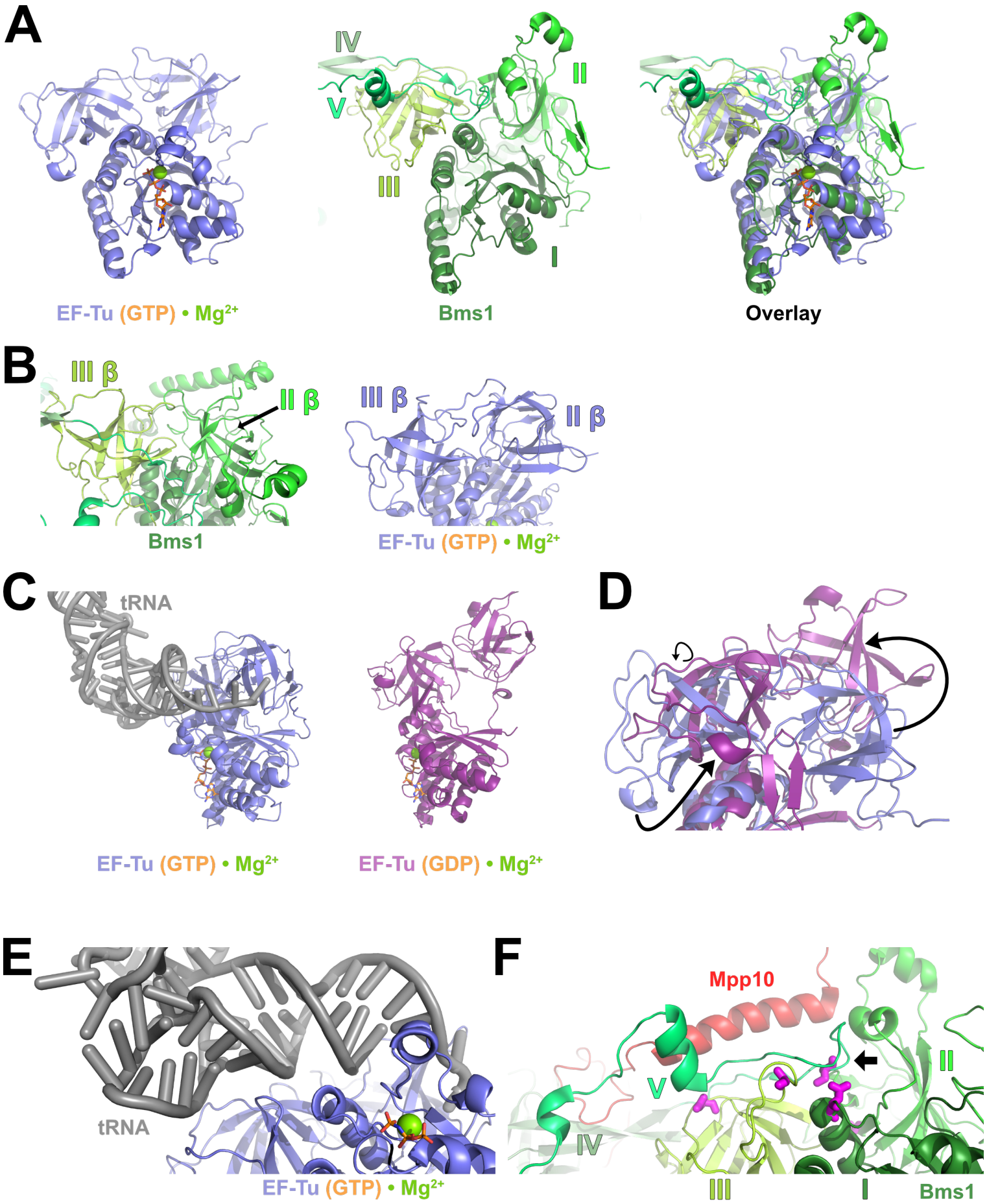

Figure S4, Black, et al 2020

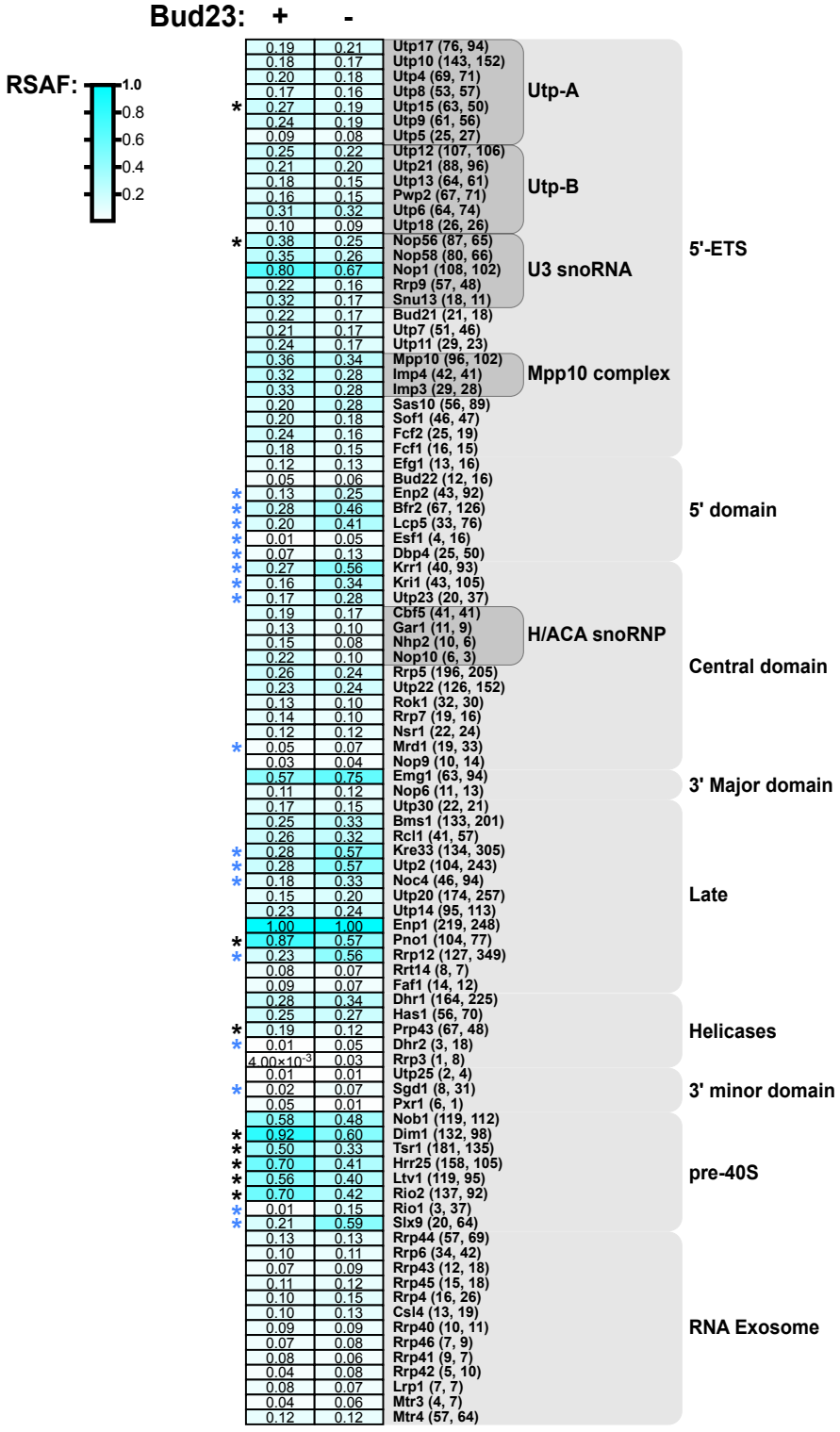

	+	-		
	0.19	0.21	Utp17 (76, 94)	Utp-A, 5'-ETS
	0.18	0.17	Utp10 (143, 152)	Utp-A, 5'-ETS
	0.20	0.18	Utp4 (69, 71)	Utp-A, 5'-ETS
	0.17	0.16	Utp8 (53, 57)	Utp-A, 5'-ETS
*	0.27	0.19	Utp15 (63, 50)	Utp-A, 5'-ETS
	0.24	0.19	Utp9 (61, 56)	Utp-A, 5'-ETS
	0.09	0.08	Utp5 (25, 27)	Utp-A, 5'-ETS
	0.25	0.22	Utp12 (107, 106)	Utp-B, 5'-ETS
	0.21	0.20	Utp21 (88, 96)	Utp-B, 5'-ETS
	0.18	0.15	Utp13 (64, 61)	Utp-B, 5'-ETS
	0.16	0.15	Pwp2 (67, 71)	Utp-B, 5'-ETS
	0.31	0.32	Utp6 (64, 74)	Utp-B, 5'-ETS
	0.10	0.09	Utp18 (26, 26)	Utp-B, 5'-ETS
*	0.38	0.25	Nop56 (87, 65)	U3 snoRNA, 5'-ETS
	0.35	0.26	Nop58 (80, 66)	U3 snoRNA, 5'-ETS
	0.80	0.67	Nop1 (108, 102)	U3 snoRNA, 5'-ETS
	0.22	0.16	Rrp9 (57, 48)	U3 snoRNA, 5'-ETS
	0.32	0.17	Snu13 (18, 11)	U3 snoRNA, 5'-ETS
	0.22	0.17	Bud21 (21, 18)	5'-ETS
	0.21	0.17	Utp7 (51, 46)	5'-ETS
	0.24	0.17	Utp11 (29, 23)	5'-ETS
	0.36	0.34	Mpp10 (96, 102)	Mpp10 complex, 5'-ETS
	0.32	0.28	Imp4 (42, 41)	Mpp10 complex, 5'-ETS
	0.33	0.28	Imp3 (29, 28)	Mpp10 complex, 5'-ETS
	0.20	0.28	Sas10 (56, 89)	5'-ETS
	0.20	0.18	Sof1 (46, 47)	5'-ETS
	0.24	0.16	Fcf2 (25, 19)	5'-ETS
	0.18	0.15	Fcf1 (16, 15)	5'-ETS
	0.12	0.13	Efg1 (13, 16)	5' domain
	0.05	0.06	Bud22 (12, 16)	5' domain
*	0.13	0.25	Enp2 (43, 92)	5' domain
*	0.28	0.46	Bfr2 (67, 126)	5' domain
*	0.20	0.41	Lcp5 (33, 76)	5' domain
*	0.01	0.05	Esf1 (4, 16)	5' domain
*	0.07	0.13	Dbp4 (25, 50)	5' domain
*	0.27	0.56	Krr1 (40, 93)	Central domain
*	0.16	0.34	Kri1 (43, 105)	Central domain
*	0.17	0.28	Utp23 (20, 37)	Central domain
	0.19	0.17	Cbf5 (41, 41)	H/ACA snoRNP, Central domain
	0.13	0.10	Gar1 (11, 9)	H/ACA snoRNP, Central domain
	0.15	0.08	Nhp2 (10, 6)	H/ACA snoRNP, Central domain
	0.22	0.10	Nop10 (6, 3)	H/ACA snoRNP, Central domain
	0.26	0.24	Rrp5 (196, 205)	Central domain
	0.23	0.24	Utp22 (126, 152)	Central domain
	0.13	0.10	Rok1 (32, 30)	Central domain
	0.14	0.10	Rrp7 (19, 16)	Central domain
	0.12	0.12	Nsr1 (22, 24)	Central domain
*	0.05	0.07	Mrd1 (19, 33)	Central domain
	0.03	0.04	Nop9 (10, 14)	Central domain
	0.57	0.75	Emg1 (63, 94)	3' Major domain
	0.11	0.12	Nop6 (11, 13)	3' Major domain
	0.17	0.15	Utp30 (22, 21)	Late
	0.25	0.33	Bms1 (133, 201)	Late
	0.26	0.32	Rcl1 (41, 57)	Late
*	0.28	0.57	Kre33 (134, 305)	Late
*	0.28	0.57	Utp2 (104, 243)	Late
*	0.18	0.33	Noc4 (46, 94)	Late
	0.15	0.20	Utp20 (174, 257)	Late
	0.23	0.24	Utp14 (95, 113)	Late
	1.00	1.00	Enp1 (219, 248)	Late
*	0.87	0.57	Pno1 (104, 77)	Late
*	0.23	0.56	Rrp12 (127, 349)	Late
	0.08	0.07	Rrt14 (8, 7)	Late
	0.09	0.07	Faf1 (14, 12)	Late
	0.28	0.34	Dhr1 (164, 225)	Helicases
	0.25	0.27	Has1 (56, 70)	Helicases
*	0.19	0.12	Prp43 (67, 48)	Helicases
*	0.01	0.05	Dhr2 (3, 18)	Helicases
	4.00×10^{-3}	0.03	Rrp3 (1, 8)	Helicases
	0.01	0.01	Utp25 (2, 4)	3' minor domain
*	0.02	0.07	Sgd1 (8, 31)	3' minor domain
	0.05	0.01	Pxr1 (6, 1)	3' minor domain
	0.58	0.48	Nob1 (119, 112)	pre-40S
*	0.92	0.60	Dim1 (132, 98)	pre-40S
*	0.50	0.33	Tsr1 (181, 135)	pre-40S
*	0.70	0.41	Hrr25 (158, 105)	pre-40S
*	0.56	0.40	Ltv1 (119, 95)	pre-40S
*	0.70	0.42	Rio2 (137, 92)	pre-40S
*	0.01	0.15	Rio1 (3, 37)	pre-40S
*	0.21	0.59	Slx9 (20, 64)	pre-40S
	0.13	0.13	Rrp44 (57, 69)	RNA Exosome
	0.10	0.11	Rrp6 (34, 42)	RNA Exosome
	0.07	0.09	Rrp43 (12, 18)	RNA Exosome
	0.11	0.12	Rrp45 (15, 18)	RNA Exosome
	0.10	0.15	Rrp4 (16, 26)	RNA Exosome
	0.10	0.13	Csl4 (13, 19)	RNA Exosome
	0.09	0.09	Rrp40 (10, 11)	RNA Exosome
	0.07	0.08	Rrp46 (7, 9)	RNA Exosome
	0.08	0.06	Rrp41 (9, 7)	RNA Exosome
	0.04	0.08	Rrp42 (5, 10)	RNA Exosome
	0.08	0.07	Lrp1 (7, 7)	RNA Exosome
	0.04	0.06	Mtr3 (4, 7)	RNA Exosome
	0.12	0.12	Mtr4 (57, 64)	RNA Exosome

Figure S5, Black, et al 2020

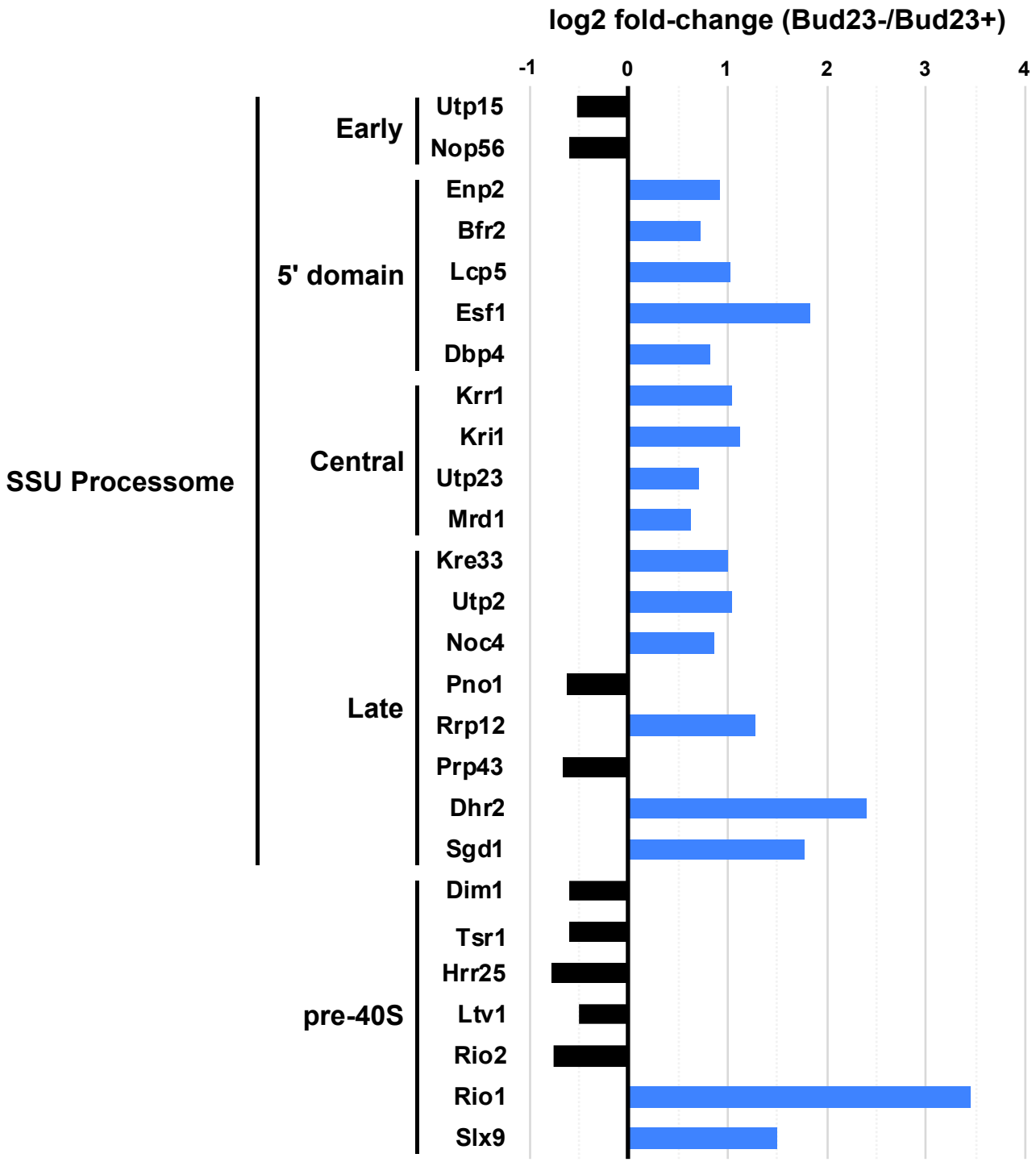

Figure S6, Black, et al 2020